UNIVERSITAS BERGENSIS

PARTICLE PHYSICS

Master Thesis

Dark Matter Searches with ATLAS and Fermi

By: Knut Dundas Morå

Supervisor: Heidi Sandaker

June 3, 2013

Thanks

Thanks, Heidi, for always taking time to talk with me, and ask me the questions I needed.
Thanks, Anna, Bjarne, Gerhaldt and Per, for friendly advice and assistance.
Thanks, everyone in the corridor, Alex, Jan, Justas, Maren, Nils, Therese, Thomas, Trygve and Ørjan, for two fun years
Thanks, Agnethe, Helge, Steffen and Zhuo, for the company and talk
Thanks, Olga, Jan and Torsten, for helping me along.

Abstract

This thesis presents Dark matter inspired searches for supersymmetry with a one-tau analysis at ATLAS, which excludes a region close to that of allowed dark matter densities at $m_0 \sim 400$ GeV, $m_{1/2} \sim 600$ GeV, $\tan\beta = 30$, $A_0 = -1200$ GeV in a "Higgs aware grid". The one tau analysis was among the first groups to constrain regions of this grid at ATLAS.
In addition, this thesis presents a computation of variables and limits in the mSUGRAparameter space, both by astrophysical experiments and other observables. The new Higgs mass and the LHCb measurement of $BR(B_s \rightarrow \mu^+\mu^-)$ impose constraints on large areas of the parameter space. However, some regions of interest are still there; the Higgs-aware grid was a good example. Also, in the region $\tan\beta = 30$,$A_0 = -2300$ GeV some promise may be found for both astro- and high-energy physics.
Last; This thesis presents an exploration of the Fermi-LAT photon data in support of an ongoing effort to investigate the planned CTAs potential. Last spring, a paper presenting a line feature at 130 GeV [70] in the Fermi-LAT spectrum was published, which has engendered an appropriately cautious response; both in view of the lack, for now, of a second experiment, as well as the importance a discovery would have.

Contents

Preface i
Abstract iii

1 Introduction **1**

2 Theory **3**

2.1 The Standard Model 3
2.1.1 The matter particles 3
2.1.2 The three forces 4
2.1.3 Gravity 5
2.1.4 The formulation of the Standard Model 5
2.1.5 The Higgs boson 5
2.1.6 Computing processes 6
2.2 Supersymmetry 7
2.2.1 Problems that SUSY solves 7
2.2.2 Particles 8
2.3 Computing processes in SUSY 8
2.3.1 Dark matter candidates 9
2.3.2 supergravity 9
Higgs mass 9
2.3.3 Dark Matter Candidates 10
2.4 Cosmology 11
2.5 Dark Matter 13
2.5.1 Rotation curves of large structures 13
2.5.2 Gravitational Lensing 16
2.5.3 Structure formation in the early universe 18

3 Experiments **20**
3.1 The Fermi Experiment 20
3.1.1 Rejecting charged particles 20
3.1.2 Good Time Intervals 21
Energy Resolution 21
Angular Resolution 22
Effective Area and Exposure 22
3.2 Dark Matter limits 24
3.3 Dark matter 24
3.4 The ATLAS experiment 25
3.4.1 The LHC accelerator 25
3.4.2 The structure of ATLAS 26
Inner Detector 26
Calorimeters 27
Muon Systems 27
3.5 Experiments and bounds 27
3.5.1 LEP 27
3.5.2 IceCube 28
3.5.3 XENON100 28
3.5.4 CTA 28
3.5.5 LHCb 29

4 Analyses **30**
4.1 Likelihood analysis of Fermi 30
4.1.1 The maximum likelihood method 30
4.1.2 Model of spectrum 31
4.1.3 Data utilized 32
4.1.4 Analysis 33
4.1.5 Limits on Cross-Sections 34
The Dark Matter Distribution 34
4.2 Computation of supersymmetric parameters 35
4.2.1 Program packages used 35
ISAJET 35
DarkSusy 36
FeynHiggs and HiggsBounds 36

4.2.2 Errors 37
top mass 37
Higgs masses 37
4.2.3 Running 37
4.3 A one-tau search for supersymmetry with ATLAS 39
4.3.1 Definitions 40
Missing Transverse Energy 40
Objects 41
4.3.2 Backgrounds 41
W, Z and top 42
QCD 43
Diboson 43
4.4 Event files 44
4.4.1 Simulated data 44
4.4.2 The Higgs Aware grid 44
4.4.3 2012 Data 45
4.4.4 Event selection 45
Trigger 45
QCD 46
4.4.5 Other Cuts 46
4.5 Computing the expected number of events 46
Pileup corrections 47
4.6 Errors 48
4.6.1 H_T cut 49
4.6.2 Expectations 50
Predicted background 50
The Higgs Aware grid 52

5 Results **55**
5.1 Fermi 55
5.2 Results of mSUGRA computations 58
5.2.1 Slices of the mSUGRA parameter space 58
$\tan\beta = 3 A_0 = 0$ GeV 58
$\tan\beta = 10 A_0 = 0$ GeV 58
$\tan\beta = 40 A_0 = 0$ GeV 59

$\tan\beta = 30 A_0 = -2300$ GeV 59
5.2.2 $\tan\beta = 30 A_0 = -2m_0$ 60
Accelerator bounds 62
Astrophysical bounds 62
Summary 63
5.3 Results from ALTAS search 67
5.3.1 Observed events 67
5.3.2 Setting a limit 68

6 Conclusions 71

A Computer Programs 80
A.1 Software Acknowledgments 80

B ATLASsupporting material 82
B.1 Signal Samples 82

List of Figures

2.1 NGC3198 rotation curve 15
2.2 The Bullet Cluster 17

3.1 A Fermi-LAT piece 21
3.2 Integrated livetime 22
3.3 Energy Resolution 23
3.4 Fermi Effective Area 24
3.5 The ATLAS detector 26
3.6 XENON100 90% exclusion from [14]. 29

4.1 The Galactic Center 33
4.2 Higgs mass vs top 37
4.3 $\tan\beta = 3, A_0 = 0$ GeV, $\mu > 0$ 38
4.4 $\tan\beta = 3\ \sigma_{\text{independent}}$ 39
4.5 Asimov significance, H_T cut 50
4.6 m_T for signal, background and data 51
4.7 $p_{T\tau}$ for signal, background and data 51
4.8 H_T for signal, background and data 52
4.9 Expected Events 53
4.10 Total cross-section 54
4.11 Uncertainty cross-section 54

5.1 The 95% confidence limit for a line signal 56
5.2 $2(\log\mathcal{L}_{\text{s+b}} - \log\mathcal{L}_{\text{b}})$ for the tested masses. 56
5.3 Best Fit 57
5.4 $\tan\beta = 3$ exclusion 58
5.5 $\tan\beta = 10$ exclusion 59

5.6 $\tan\beta = 40$ exclusion 60
5.7 $\tan\beta = 3$ exclusion 61
5.8 m_H 61
5.9 $m_{\tilde{\tau}}$ and $m_{Neutralino}$ 62
5.10 $B_s \to \mu^+\mu^-$ 63
5.11 caption 64
5.12 $\langle\sigma v\rangle_{\gamma\gamma}$ 64
5.13 $\langle\sigma v\rangle$ 65
5.14 $m_{\tilde{\tau}}$ and $m_{Neutralino}$ 65
5.15 $m_{\tilde{\tau}}$ and $m_{Neutralino}$ 66
5.16 Exclusion contours for the Higgs aware grid 66
5.17 The same as Figure 5.16, but with a higher m_0 resolution. 67
5.18 H_T 68
5.19 ATLAS exclusion contour 69
5.20 exclusion in grid 70

List of Tables

2.1 The leptons, with masses[60] and charges 4
2.2 The quarks, with masses[22] and charges. Note that light quarks are estimates, ... 4
2.3 caption here 4
2.4 Supersymmetric partners of standard model particles 8
2.5 The balance of energy densities in the current universe 13

4.1 Cut-flow for the kinematic cuts defining the SR after the baseline event selection. All numbers are from MC scaled to an expected data luminosity of 20.7fb^{-1}with scale factors applied to top, W+jets and Z+jets, except for the final estimate of QCD events. The errors are statistical only. 52
4.2 Number of expected events at 20.7fb^{-1} that are expected to pass the analysis cuts. 53

5.1 Cut-flow for background, data and some signal points. The expected numbers of events for all standard model backgrounds and for the example of one GMSB and two mSUGRA parameter space points correspond to an integrated luminosity of 20.7fb^{-1}. 67

B.1 List of MC samples for the SUSY signal in the mSUGRA Higgs boson-aware grid. Masses are quoted in GeV. Another 105 samples with $m_0 > 2000$ GeV have been generated, but they are far away from the region where the $\tilde{\tau}$is the NLSP. 83
B.2 List of nine additional MC samples close to the coannihilation region for the SUSY signal in the mSUGRA Higgs boson-aware grid. Masses are quoted in GeV. 84

1

Introduction

hDark matter is currently in the exiting position of being a mystery that might soon be revealed. Any confirmation would raise the impetus to produce and study the particle in a particle accelerator. Part of my work has therefore been to examine the possibility or degree of overlap between the reach of accelerators and astrophysical dark matter detection experiments.

To relate the two, I have focused on the mSUGRA supersymmetric models. Computing cross-sections and masses provide a glue between the different experiments by relating them all to the same space.

The main effort in my thesis is divided into three parts, all dealing with dark matter

- I have studied data from the Fermi-LAT telescope, that last year reported a line in their photon spectrum to support work done on the planned CTA telescope. If the line turns out to be confirmed by other experiments, this will be of major importance.
- I have computed properties of slices of the mSUGRAparameter space,
- And I participated in an ATLASsearch for supersymmetry, in which an mSUGRAslice was among the grids considered, and the limit excluded regions of acceptable relic

density.

In the following text, I will start with a very short introduction to the standard model and supersymmetry, before reviewing some of the evidence for dark matter. After this, I will go through the work I have done, and afterwards the results.

2

Theory

2.1 The Standard Model

The current understanding of particle physics is gathered in the Standard Model. It has withstood experimental scrutiny for around 30 years, and recently the last particle in the standard model- the Higgs boson- was discovered at CERN[62].

2.1.1 The matter particles

Matter particles are all spin 1/2-particles in the standard model They are split in two families; the leptons and the quarks. As matter particles, they have an intrinsic angular momentum that will be observed to be $\pm 1/2$, whatever the direction of the measurement. Spin 1/2 particles, fermions, follow Fermi-Dirac statistics; two identical particles cannot have the same quantum numbers. All the particles have an antiparticle- a mirror image with the same mass, but opposite helicity and charges.

The leptons interact with the electroweak forces. There is the electron e, muon μ and tau τ, all of which interact similarly, only with different masses. In addition, each of them has a corresponding neutrino; a light, neutral particle that only interacts with the weak force.

Table 2.1: The leptons, with masses[60] and charges

1st gen		2nd gen		3rd gen	
electron,	e	muon,	μ	tau,	τ
0.511MeV,	$+1$	105.7MeV,	$+1$	1.78×10^3MeV,	$+1$
e neutrino,	ν_e	μ neutrino,	ν_μ	τ neutrino,	ν_τ
~ 0,	0	~ 0,	0	~ 0,	0

Table 2.2: The quarks, with masses[22] and charges. Note that light quarks are estimates,

1st gen		2nd gen		3rd gen	
up,	u	charm,	c	top,	t
$2.3^{+0.7}_{-0.5}$ MeV,	$+2/3$	1.275 ± 0.025GeV,	$+2/3$	$173.5 \pm 0.6 \pm 0.8$ GeV,	$+2/3$
down,	d	strange,	s	bottom,	b
$2.8^{+0.7}_{-0.3}$ MeV,	$-1/3$	95 ± 5MeV,	$-1/3$	4.18 ± 0.03GeV,	$-1/3$

Quarks

2.1.2 The three forces

In the Standard Model, forces are mediated by particles. The three forces of the standard model are the electromagnetic, weak and strong force. The electromagnetic force couples to electric charge, and is mediated by photons. The Weak force is carried by the $W^\pm$ and Z bosons, and is confined to short ranges due to their large masses [64, p.13]. In the end comes the gluons that interact with color charge, which only quarks and gluons carry.

Table 2.3: caption here

Force	Electromagnetic	Weak	Strong
Boson	γ	Z^0,$W^\pm$	$g \times 8$
Mass[22]	0	91.1876 GeV, 80.385 GeV,0	

2.1.3 Gravity

The fourth force we observe in nature is gravity. No attempts to combine gravity and the other forces in one framework has so far succeeded. The strength of gravity is vastly smaller than the other forces; $G_N = 6.7 \times 10^{-11}\,\mathrm{N\,m^2\,kg^{-2}}$, or $G_N = 6.7 \times 10^{-45}\,\mathrm{MeV^{-2}}$[60], and ignoring it for processes below these massive[1] scales is an excellent approximation.

2.1.4 The formulation of the Standard Model

The Standard model is formulated in terms of field theory, with a Lagrangian that governs the equations of motion of the fields. It turns out that there are operations you can do to the fields which leave the Lagrangian and the equations of motion unchanged. This is termed a symmetry of the Lagrangian, and an example is the freedom to choose a complex phase for a field that is always multiplied with its conjugate. If one further requires that the phase should be able to change as a function of space, derivatives acting on the fields will act on the phase transformation, adding a term to the Lagrangian. It turns out that to balance this out, a vector field is needed that will transform to keep the Lagrangian invariant. Different symmetries lead to different physics. The standard model is built on three symmetries; $U(1)_Y \times SU(2)_L \times SU(3)$. The first is akin to the photon, the $SU(2)_L$ transforms in isospin and acts only on left-handed particles, and SU(3). The number of vector fields needed is related to the symmetry; so a $U(1)$ will lead to one vector boson field $\boldsymbol{B}$., the $SU(3)$ has three: $W^+, W^- and W^0$ and a $SU(3)$ has eight g. The B and W^0 bosons mix, and the result is a γ and the Z_0.

2.1.5 The Higgs boson

Simple mass terms for the weak bosons will not be invariant under SU(2) transformations, which only acts on the left handed spinors. Fermion masses are similarly compromised. What is needed is a mass term that will combine left-handed isospin doublets with right-

---

[1] sorry

handed isospin singlets, as well as provide a mass to the heavy vector bosons. [55] [p.389-449]. The Higgs mechanism provides such an object- it introduces a scalar isospin doublet $\boldsymbol{\phi}$ that interacts with the vector bosons. Adding a potential $V = \mu^2|\boldsymbol{phi}|^2 + \lambda|\boldsymbol{phi}|^4$, with $\mu^2 < 0$[2] means that the state of lowest energy is when $|\boldsymbol{\phi}| = \sqrt{-mu^2/(2\lambda)}$. This is the famous Mexican hat potential; as the field may have any complex phase, the minimum lies in the rim of the hat. Perturbations to the field may be either in the phase, which does not change the potential, or it may be a perturbation in the absolute value of the field. When the Higgs field interacts with the vector bosons, the Lagrangian will include a term where the vacuum expectation value of the Higgs field is multiplied by a mass term. From a isospin scalar field and massless vector fields, the Higgs field condenses into the rim of the hat. At the outset, the Higgs field has four degrees of freedom- a complex field up and down. Using the freedom to choose a gauge, it may be seen that the three vector bosons gain a mass, and thereby gaining one degree of freedom each, since massive spin-1 bosons may have a longitudinal spin. In addition, a field corresponding to an oscillation to and fro in $|\phi|$ represents a massive scalar particle- the Higgs boson. The condensation of a Higgs field, where an arbitrary but fixed direction in isospin and phase is chosen is referred to as spontaneous symmetry breaking [55, p.410].

The matter particle masses may be included by Youkawa couplings; $\propto m\psi\theta\psi$. In addition to the mass term, the Higgs particle, the oscillations in ϕ, will have interactions with the matter particles proportional to their mass. Finally, the Higgs may interact with itself by threes and fours.

On the fourth of June 2012, the ATLASand CMS experiments announced the discovery of a Higgs boson with mass 126.5 GeV[62]. The current ATLAS combined measurement of the mass is $125.5 \pm 0.2(\mathrm{stat}^{+0.5}_{-0.6}(\mathrm{say's})$ GeV[1].

2.1.6 Computing processes

When one wishes to calculate the probability of a quantum mechanical process, it turns out to be an infinite sum of powers of the interaction Hamiltonian[55, p.92]. Electromagnetic interactions, for example, are dampened by a factor $\alpha \approx 1/137$ for each power.

---

[2] λ must be positive lest the lowest energy state should be at $|\boldsymbol{phi}| = \infty$

Perturbation theory is then to truncate this infinite series as higher order terms become small. Furthermore, the results of the series may be formulated more intuitively in terms of Feynman diagrams, where lines represent particles, and vertices correspond to the couplings. All possible diagrams with one vertex that incorporates the in- and out-going particles will together represent the first order term in perturbation theory. An intuitive way of putting together the different levels is through Feynman diagrams. The Feynman rules incorporate propagators- they are inserted on all internal lines.

For spin 0, for example, the propagator is simple: $\frac{i}{q^2-m^2}$ Where q is the momentum along the internal line, and m the mass. For spin 1/2 particles, the propagator is somewhat: $\frac{i(\not{q}+m)}{q^2-m^2}$.

However, Feynman graphs are only an approximation to nature. There are an almost infinite number of paths from any given input state to the output. The effects of all this activity is observable- the strength of the electromagnetic force changes at very high momentum transfers, as does the other couplings. The couplings converge and almost meet at some hard energy scale, leading to speculation if this could mean that at the very highest energy level, all forces are one and the same[64, p.99]

2.2 Supersymmetry

Supersymmetry is one of the best-studied models of new physics. It introduces operators will transform a fermion into a boson, and the other way around, doubling the number of particles. No superpartner has been observed, and therefore they must, if they exist be heavy, and supersymmetry somehow broken.

2.2.1 Problems that SUSY solves

Supersymmetry solves some of the less photogenic sides of the standard model:

- Most SUSY models will have a dark matter candidate

- A unification of the forces at the GUT scale is possible due to changes in the running couplings[22, p. 1420]
- The Higgs mass would be affected if there were heavier particles it could couple to. Supersymmetry gives each fermion its bosons and vice versa. In this case, the loops will cancel out, and the Higgs not be [44, p412].

2.2.2 Particles

Each standard model particle has a supersymmetric partner, sparticle, with opposite statistics. Superpartners of fermions get an s, while those of the bosons get an -ino.

quarks	u c t	d s b	spin 1/2
leptons	e μ τ	νs	spin 1/2
gauge bosons	γ, W, Z	g	spin 1
scalar bosons	h	H	
gauginos	$\tilde{\chi}^0_1$,$\tilde{\chi}^0_2$, $\tilde{\chi}^0_3$, $\tilde{\chi}^0_4$, $\tilde{\chi}^\pm_1$, $\tilde{\chi}^\pm_2$	$\tilde{g}$	spin 1/2
sleptons	$\tilde{e}\tilde{\mu}\tilde{\tau}$	$\tilde{\nu}$s	spin 0
squarks	$\tilde{u}$ $\tilde{s}$ $\tilde{t}$	$\tilde{d}$ $\tilde{c}$ $\tilde{b}$	spin 0

Table 2.4: Supersymmetric partners of standard model particles

Where the $\tilde{\chi}^0$s are the linear combination resulting in mass eigenstates for the superpartners of the γ and Z[3] as well as the two neutral higgses. The same applies for the $\tilde{\chi}^\pm$s, partners of the $W^\pm$ and a charged Higgs doublet.

2.3 Computing processes in SUSY

One of the virtues of supersymmetry is its ease of

---

[3] or B and W_3

2.3.1 Dark matter candidates

It is common to impose R-parity on supersymmetric models. This ensures that supersymmetric particles are pair-produced at accelerators. It is possible to include interaction terms in the supersymmetric Lagrangian that violate R-parity. However, these will make proton decay possible, which is excluded to 1×10^{29} y[22, p.1256][23] The stability over very long timescale makes for an attractive dark matter candidate. Typical examples are a neutralino or a gravitino. At some point during the Big Bang, all heavier SUSY particles would have fallen out of equilibrium and decayed into the lightest supersymmetric particle. As both these particles are weakly interacting as well, making them excellent candidates, as I shall show later in the case of neutralino.

2.3.2 supergravity

If one demands a local supersymmetry, as one demands a local symmetry in the standard model when deriving the forces from the Lagrangian. In the case of supersymmetry, however, demanding a local supersymmetry will result in a spin-3 graviton

Higgs mass

in the MSSM, at tree level, the Higgs mass is bounded by the Z mass, lower than the bound of 114.4 GeV found at LEP[60, p.10]. Radiative corrections may give considerably higher Higgs masses; as in the case of a large stop mass[22, p.1426]:

$$m_h^2 \lesssim m_Z^2 + \frac{3g^2 m_t^4}{8\pi^2 m_W^2} \left[\ln(M_S^2/m_t^2) + \frac{X_t^2}{M_S^2} \left(1 - \frac{X_t^2}{12 M_S^2} \right) \right] \tag{2.1}$$

Where $M_S = \frac{1}{2}(M_{\tilde{\tau}_1}^2 + M_{\tilde{\tau}_2}^2)$ and $X_t \lesssim A_t - \mu \cot\beta$.

2.3.3 Dark Matter Candidates

Multiple proposals have been put forth to explain excessive rotation curves of galaxies. Zwicky[73] proposed extra, dark, matter to fit the rotation of the Coma Cluster. In addition to dark matter, it has been proposed to modify Newton's r^{-2}-law of gravity at large distances. The Bullet cluster shows that the effects of dark matter does not simply track the visible matter distribution would seem to disfavor such a model. As detailed in section 2.5.2, MACHOs also seem unable to explain the observations. Neutrinos are dark matter, but their masses would have to be on the order of some eV, far higher than the $> 0.1\,\text{eV}$ that is suggested by neutrino oscillations[64, p.167]. Furthermore, neutrinos would have been relativistic around decoupling, and would dampen out fluctuations. The Planck experiment finds that the number of relativistic degrees of freedom are $N_eff = 3.30 \pm 0.27$, and limits the sum of masses to > 0.23[7].

A candidate for dark matter must be neutral, heavy (cold) enough to form structures around decoupling. It must be stable on cosmological timescales, and cannot interact much with ordinary matter. In addition, the model must be compatible with the observed relic density.

Axions are the result of introducing an additional U(1) symmetry to explain the lack of strong CP violation[60, p.218]. Through non-perturbative interactions with gluons, they gain a small mass [28]. They also couple to two photons, through a triangle diagram with a quark. Limits have been set at $m_a < 0.01\,\text{eV}$ by considering stars cooling by $\gamma\gamma \rightarrow$ axion . In addition, to make up the observed dark matter, the axion would have to weigh in excess $6 \times 10^{-6}\,\text{eV}$[28].

Weakly interacting massive particles, WIMPs, also fit the above requirements. As with neutrinos, they will be frozen out as the cross-section drops with temperature, and the mean free path $1/\left(N < \sigma v >\right)$ approaches the size of the universe $\sim 1/H$;

$$1/N \langle \sigma v \rangle < \qquad 1/H \tag{2.2}$$

The expected number density N of non-relativistic fermions is $\propto (mT)^{3/2}e^{-m/T}$[64, p.140], and the Hubble constant $\propto T^2/M_{\mathrm{PL}}$, giving an equation for freeze-out. It is clear that if the cross-section does not increase with dropping temperature, the WIMP will be frozen out. Assuming a typical weak cross-section of $G_F^2M^2$, one can compute the temperature;

$$(mT)^{3/2}e^{-m/T}G_F^2M^2 = T^2/M_{\mathrm{PL}}K \tag{2.3}$$

Where K is a constant of the order 100[64, p.171]. Where the freeze-out temperature is characterized by $P = m/T$. The equation may be solved numerically, and by using Newtons method, I find P ranges from roughly $15 - 40$ from $m = 1 - 1000\,\mathrm{GeV}$ Thus, the number density becomes;

$$N \sim \frac{T^2}{M_{\mathrm{PL}}\langle\sigma v\rangle} \tag{2.4}$$

At decoupling, or, today stretched by $(1+z)^{-3}$. The CMB temperature is $\propto 1/(1+z)$, so the density today at T_0 is:

$$N_0 \sim (T_0/T)^3\frac{T^2}{M_{\mathrm{PL}}\langle\sigma v\rangle} \tag{2.5}$$

$$\rho_0 = mN_0 \sim PT_0^3M_{\mathrm{PL}}\langle\sigma v\rangle \tag{2.6}$$

$$\rho_0 \sim \frac{6\times10^{-31}\,\mathrm{GeV\,s^{-1}}}{\langle\sigma v\rangle} \tag{2.7}$$

Using ρ_c from section 2.15, and $mv^2/2 = 3T/2$ giving $v \sim 0.3$, one finds that a cross-section of the order of weak interactions will close the universe[64, p.173]:

$$\Omega_{\mathrm{DM}} \sim \frac{1\times10^{-25}\,\mathrm{cm^3\,s^{-1}}}{\langle\sigma v\rangle}. \tag{2.8}$$

2.4 Cosmology

The study of the structure and history of the universe has led to a pleasing combination of particle physics and astrophysics. Observations are consistent with a universe that starts out very hot- enough to produce any standard model particle in its earliest times. Edwin

Hubble discovered a redshift in distant galaxies that increased linearly with distance [47]. He interpreted this as a Doppler effect, shifting the photon energy:

$$\frac{E'}{E} = \sqrt{\frac{1-v}{1+v}} \sim_{v \ll 1} 1 - v \tag{2.9}$$

$$H = rv \tag{2.10}$$

Where the Hubble constant relates velocity v and distance r. $H = (67.4 \pm 1.4)\,\mathrm{km\,s^{-1}\,Mpc^{-1}}$[7]. $H = h100\,\mathrm{km\,s^{-1}\,Mpc^{-1}}$ is a common convention. For larger redshifts than Hubble considered, not only Doppler shifts, but gravitational redshifts are relevant[64, p.110]. Therefore, the redshift z is used:

$$\frac{E'}{E} = \frac{\lambda}{\lambda'} = 1 + z \tag{2.11}$$

If the Earth is not situated in a special spot in the universe, the explanation for everything moving away from the Earth must be that the universe is expanding uniformly. The ratio of distances at a time t and now in terms of redshift becomes;

$$\frac{R(0)}{R(t)} = 1 + z \tag{2.12}$$

and the Hubble constant will give the expansion:

$$H = \frac{\dot{R}(t)}{R(t)} \tag{2.13}$$

Assuming a homogeneous and isotropic universe, Einsteins field equations imply:

$$H^2 = \frac{8\pi G_N}{3}\rho_{\text{tot}} - \frac{k}{R^2} \tag{2.14}$$

Where the energy density ρ, with it's dependence on R, as well as a curvature term k determines the evolution of H. The curvature may be $0, 1, -1$, denoting a flat (euclidean), closed or open geometry. The matter density that will close the universe today is $\rho_c = \frac{3}{8\pi G_N} H^2$. how close one is to the critical density today is expressed as the closure Ω:

$$\Omega_i = \frac{\rho_i}{h^2 1.88 \times 10^{-29}\,\mathrm{g\,cm^{-3}}} \tag{2.15}$$

Current experiments suggest the universe is flat. In addition to ordinary matter and a redshifted microwave background, the current understanding of the universe includes dark matter, that is only detected through its gravity, and dark energy, that causes the universe to accelerate. The energy densities are tabulated below.

Table 2.5: The balance of energy densities in the current universe

Baryonic matter	Ω_b	$0.049\,06 \pm 0.000\,60$[7]
Dark matter	Ω_DM	0.2667 ± 0.0060[7]
Cosmic Microwave Background	Ω_CMB	4.8×10^{-5}[60]
Dark Energy	Ω_Λ	$0.685^{+0.018}_{-0.016}$[7]

As the universe expands, the densities will decrease; the matter and dark matter densities today go as: $\propto (R_0/R_z^{-3} = (1+z)^{-3}$, while radiation will drop as $\propto (R_0/R_z^{-4} = (1+z)^{-4}$. The mass of matter is only diluted by an increasing volume, while radiation, while relativistic particles may be envisioned as having their wavelength stretched as well.

2.5 Dark Matter

The indications that there exists dark matter in the universe is strong, and based on multiple lines of evidence or indication:

2.5.1 Rotation curves of large structures

The gravitational field $\boldsymbol{g}(\boldsymbol{r}) \equiv \boldsymbol{F}_\mathrm{grav}/m$ is governed by the equation (2.16a). By using Gauss' theorem, this is equivalent to equation (2.16b), where the left integral is a two-dimensional closed integral of the inner product of the field and a normal vector $\hat{\boldsymbol{n}}$ to the surface, while the right side is a three-dimensional integral over the volume bounded by the surface. Assuming a spherically symmetric distribution, one gets (2.5.1)

$$\nabla \cdot \boldsymbol{g}(\boldsymbol{r}) = 4\pi\rho(\boldsymbol{r}) \tag{2.16a}$$

$$\oiint \boldsymbol{g} \cdot \hat{\boldsymbol{n}} \mathrm{d}A = 4\pi \iiint \rho \mathrm{d}V \tag{2.16b}$$

$$\boldsymbol{g}(\boldsymbol{r}) = -\hat{\boldsymbol{r}} G_N \frac{M_{<\mathrm{r}}}{r^2} \tag{2.16c}$$

The virial is defined as a sum over all particles[40][p.83].

$$G = \sum_i \boldsymbol{p}_i \cdot \boldsymbol{r}_i \tag{2.17}$$

Where each particle has a position $\boldsymbol{r}_i$, mass m_i and momentum $\boldsymbol{p}_i = \dot{\boldsymbol{r}}_i m_i$. Differentiating G, one gets;

$$\frac{\mathrm{d}G}{\mathrm{d}t} = \sum_i (\dot{\boldsymbol{r}}_i \boldsymbol{p}_i + \boldsymbol{r}_i \dot{\boldsymbol{p}}_i) \tag{2.18}$$

$$\frac{\mathrm{d}G}{\mathrm{d}t} = \sum_i \left(2|\boldsymbol{p}_i|^2/2m + \boldsymbol{r}_i \boldsymbol{F}_i\right) \tag{2.19}$$

since $\boldsymbol{F} = \dot{\boldsymbol{p}}$. Taking the time average, and noting that the first term is the kinetic energy T;

$$\frac{1}{t}\int_0^t \frac{\mathrm{d}G}{\mathrm{d}t} = 2\overline{T} + \overline{\sum_i \boldsymbol{r}_i \boldsymbol{F}_i} \tag{2.20}$$

For a bound system, the virial is finite. Therefore, in the limit $t \to \infty$, the left hand integral above will tend to 0, giving the result;

$$\overline{T} = -\frac{1}{2}\overline{\sum_i \boldsymbol{r}_i \boldsymbol{F}_i} \tag{2.21}$$

Assuming the gravitational force from equation :

$$\overline{T} = -\frac{1}{2}\overline{\sum_i \frac{G_N m_i M_{<r}(r)}{r}} \tag{2.22}$$

The right hand sum is the potential energy of the sum, and one observes that by measuring the velocity distribution of a collection of orbiting objects, one can deduce the gravitational potential, and thus the mass.

The distribution of light from spiral galaxies suggests that most of the mass is concentrated in the center. In the limit that all the mass is in the center, the velocity of a circular orbit further out will be:

$$\frac{mv(r)^2}{2} = \frac{G_N M_{\text{center}}}{r} \tag{2.23}$$

$$v(r) = \sqrt{\frac{G_N M_{\text{center}}}{r}} \tag{2.24}$$

Thus one expects the velocities in the outer disk to drop off as $r^{-\frac{1}{2}}$.

The Doppler shift of spectral lines measures the velocity along the line of sight. By looking at a system that has its angular momentum perpendicular to the line of sight, such as looking at a disk galaxy edge-on, a rotation curve may be constructed that will reflect the matter distribution of the system.

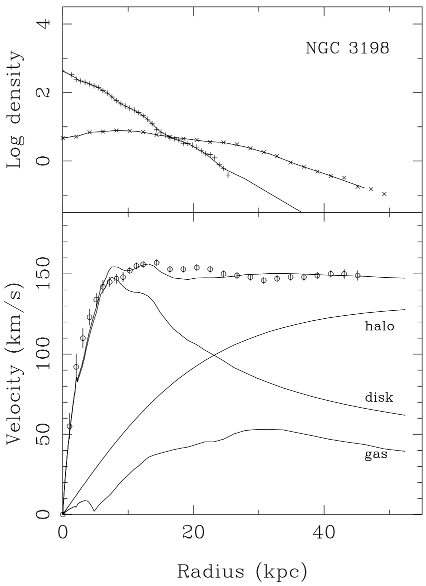

Figure 2.1: An example of a Density(above) and rotation curve of the galaxy NGC 3198 from [24], using results from the Palomar-Westbork survey [71] and Hydrogen line observations from Westbork and the Very Large Array[20].

Figure 2.1 shows one such rotation curve, with the contributions expected from the galactic disc, dust clouds and residual attributed to a dark matter halo. It is clear that the observed stars and gas cannot account for the rotation curve.

2.5.2 Gravitational Lensing

Light travel in straight lines in the curved space of general relativity. If the light path is parametrised as $x^i(s)$, where roman indices run from 1 to 3, the equation of motion is[59][p222]:

$$\frac{\mathrm{d}^2 x^j}{\mathrm{d}s^2} = -2\frac{\partial \phi}{\partial x^j} + 2\frac{\partial \phi}{\partial x^k}\frac{\mathrm{d}x^j}{\mathrm{d}s}\frac{\mathrm{d}x^k}{\mathrm{d}s} \tag{2.25}$$

Where ϕ is a weak gravitational potential. Assuming a glancing trajectory, and a small deflection, $x = s, y = y_0, z = 0$. The resulting equation for y and z becomes;

$$\frac{\mathrm{d}^2 y}{\mathrm{d}s^2} = -2\frac{\partial \phi}{\partial y} \tag{2.26}$$

$$\frac{\mathrm{d}^2 z}{\mathrm{d}s^2} = -2\frac{\partial \phi}{\partial z} \tag{2.27}$$

Where the last term of equation (2.25) vanishes due to the y and z being constant. Inserting the potential $\phi = -G_N \frac{M}{\sqrt{x^2+y^2+z^2}}$, and rotating the path so that $z = 0$;

$$\frac{\mathrm{d}^2 y}{\mathrm{d}s^2} = -2G_N M \frac{y}{(x^2+y^2)^{3/2}} \tag{2.28}$$

$$\tag{2.29}$$

The difference in $\frac{\mathrm{d}y}{\mathrm{d}x} = \frac{\mathrm{d}y}{\mathrm{d}s}\frac{\mathrm{d}s}{\mathrm{d}x} = \frac{\mathrm{d}y}{\mathrm{d}s}$ $(x = s)$ before and after the lensing measures the change in angle. Integrating the above equation, one gets;

$$\Delta \frac{\mathrm{d}^2 y}{\mathrm{d}s^2} = -\frac{2G_N M}{y_0}\int_{-infty}^{infty} \frac{\mathrm{d}s/y_0}{((s/y_0)^2+1)^{3/2}} \tag{2.30}$$

$$\Delta \frac{\mathrm{d}^2 y}{\mathrm{d}s^2} = \frac{-4G_N M}{y_0} \tag{2.31}$$

The last equation expresses the angular deflection, which, as one would expect is negative; gravitational lenses are convex. Unlike real lenses, it should be noted that the deflection is achromatic. This may be used to discriminate lensed images from other objects.

4

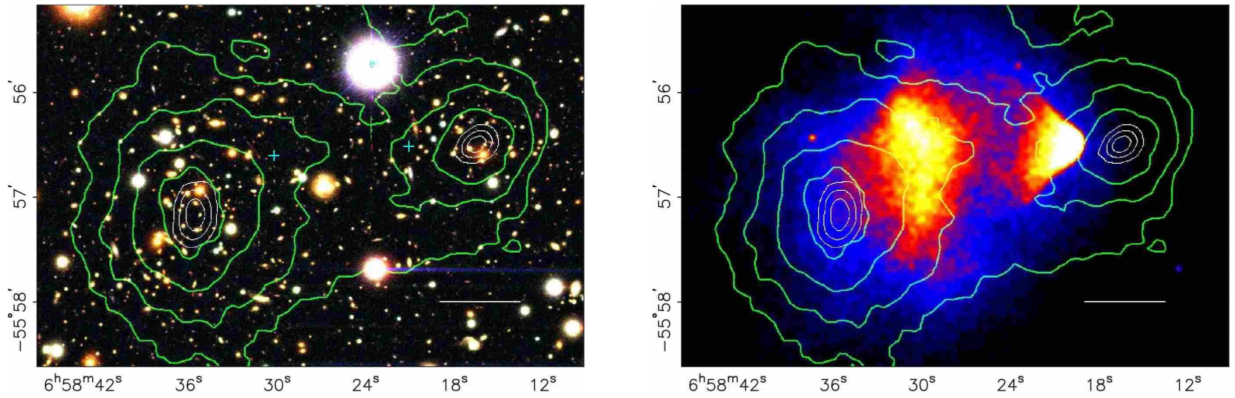

Figure 2.2: The Bullet Cluster, 1E0657-558, imaged in visual light to the left and X-rays to the right from Clowe *et al*[31]. The optical image is from the Magellan telescope, and the X-ray image from the Chandra experiment. The green contours represents the amount of distortion due to lensing. The lensing map was compiled from many optical image sets; In addition to Magellan, the ESO/MPG telescope and the Very Large Telescope' as well as the Hubble space telescope.

Using the distortion of galaxies behind the lens, one may construct an image of the matter distribution that is bending the light. This was famously done with the Bullet cluster[31], where two galaxy clusters have collided and passed through each other. The hot gas can be seen in the X-ray image to the right in figure2.2. A shock wave from the collision is clearly seen. Clowe et al.[31] report an 8σ offset between the center of mass deduced by lensing and the visible matter derived by X-ray and optical observations. In contrast to e.g. rotation curves, this observation demonstrates that dark matter may be separated from visible matter.

In addition to stars and clouds of gas, we know that planets, asteroids and even black holes contribute to the mass of a galaxy. In the context of dark matter, they are termed MACHOs; Massive Compact Halo objects. Microlensing is a technique to measure the density of MACHOs. A massive object close to the line between the earth and a light source will bend more light to the earth. Since the amplification is strongly dependent

---

[4] It is often stated that Newtonian gravity predicts half the deflection that general relativity does. However, this supposes that one treats photons as particles with a gravitating mass equal to the energy, and that it obeys Newtons law $\boldsymbol{F} = m\boldsymbol{a}$. Maxwell's laws were the accepted description of light waves before Einstein started his work. They do not include any interaction with gravity.

on the distance between the lensing object and the line of sight, this results in a time-dependent amplification of the source. As noted above, the achromatic nature of the amplification is used to distinguish this from other variable objects. The simple case of a uniform field of matter objects between the Earth and source gives the optical depth, or the probability of scattering given by the density of lensing material ρ and source distance D_{source}[64][p. 163]:

$$P_{\text{lensing}} = \frac{2}{3}\pi G_N D^2_{\text{source}}\rho \tag{2.32}$$

This probability is very low for galactic densities, and the OGLE experiment report $P_{\text{lensing}} = (1.30 \pm 1.01) \times 10^7$ and compute that 2% of the galactic halo is constituted by MACHOs[72]. Thus, these objects cannot explain the observed rotation curves.

2.5.3 Structure formation in the early universe

In the very early universe, the temperature was high enough that even heavy particles were relativistic. As the universe expands in size R and cools, the radiation density drops as $\rho \propto R^{-4}$, while matter drops as R^{-3}[64, p.119]. At some point, the matter density will dominate over radiation. As the temperature decreased further, nuclei and electrons combined into neutral atoms, decoupling matter and radiation. After this point, a fluctuation in matter density would not be opposed by radiation, and structures may form. The photons survive, redshifted to the cosmic microwave background. The ratio of baryon and photon energy density is equal at a redshift of $z \approx 900$. If matter started to clump this late, galaxies would not have had time to form[64, p.139, p.213]. If one includes dark matter, the universe is dominated by the matter density earlier, at redshifts of ≈ 3000. Dark matter does not interact with photons, and so the clumping of dark matter would not be opposed by the radiation pressure that affects baryonic matter. If dark matter has a significant mass compared to the This means that at the last scattering, the large scale structures of the galaxy have already formed their dark matter skeleton, upon which ordinary matter will clump.

The cosmic microwave background is not uniform. Small anisotropies provide a picture of the properties of density waves that oscillated in the plasma before the last scattering. By fitting to the correlation spectrum of the CMB, the Planck satellite has measured the cold dark matter density to be $\Omega_c h^2 0.1196 \pm 0.0031$[7]. In comparison, the best fit baryonic matter density is $\Omega_m h^2 0.1196 \pm 0.0031$.

3

Experiments

3.1 The Fermi Experiment

The Fermi Large Area Telescope (LAT) is a satellite-borne gamma ray telescope, capable of imaging the sky from 20 to 300 GeV. At these energies, photons will pair-convert to e^+e^- pairs as it interacts with matter. It reconstructs the photon direction using a tracker made of 18 layers of silicon strip detectors and tungsten converter material. After the tracker, CsI(Tl) crystal calorimeters measure the energy.

3.1.1 Rejecting charged particles

The LAT is surrounded by an anti-coincidence detector, the ACD. Plastic scintillator plates detect charged particles impinging on the instrument. The plates are segmented, so that charged primary particles may be distinguished from secondaries[12]. An estimator, P_{all} represents the probability of an accepted event being a real photon. For the class of photons, P_{all} is required to exceed a curve giving a $> 2\%$ chance of a fake photon at > 0.9 GeV, and $> 1\%$ at > 2.4 GeV[6][58].

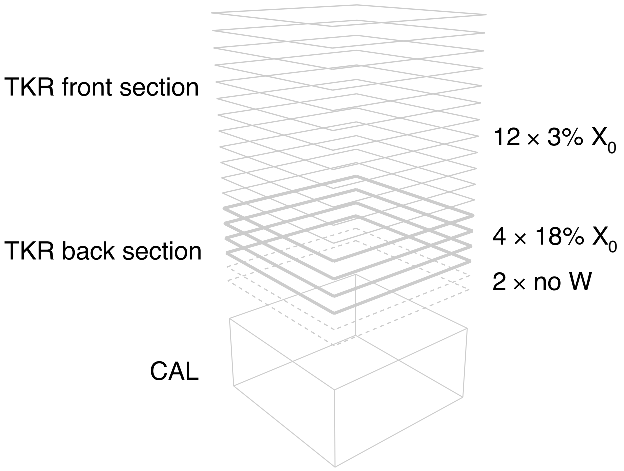

Figure 3.1: Fermi schematic
Schematic of one of 16 towers of the LAT tracker and calorimeter. The ACD is laid outside them. Taken from [6]

3.1.2 Good Time Intervals

As the LAT orbits, the times it has spent with a particular spot of the sky in its field of view is summed up to compute the total livetime. The Fermi Science Tools *gtmktime* takes the spacecraft file that the Fermi collaboration provides. The spacecraft file contains the pointing history of the satellite, as well as information of all downtime, such as when the craft passes the South Atlantic Magnetic Anomaly[12]. The result is a *Healpix*[43] grid, as illustrated in figure3.2:

Energy Resolution

The energy resolution of the LAT is defined in terms of 68% containment. The resolution degrades at very high or low energies, as the photons either do not deposit enough energy in the tracker, or the calorimeter does not contain the shower[6]. The energy dispersion is not used in the standard Fermi likelihood tools. A plot of the energy dispersion is included below:

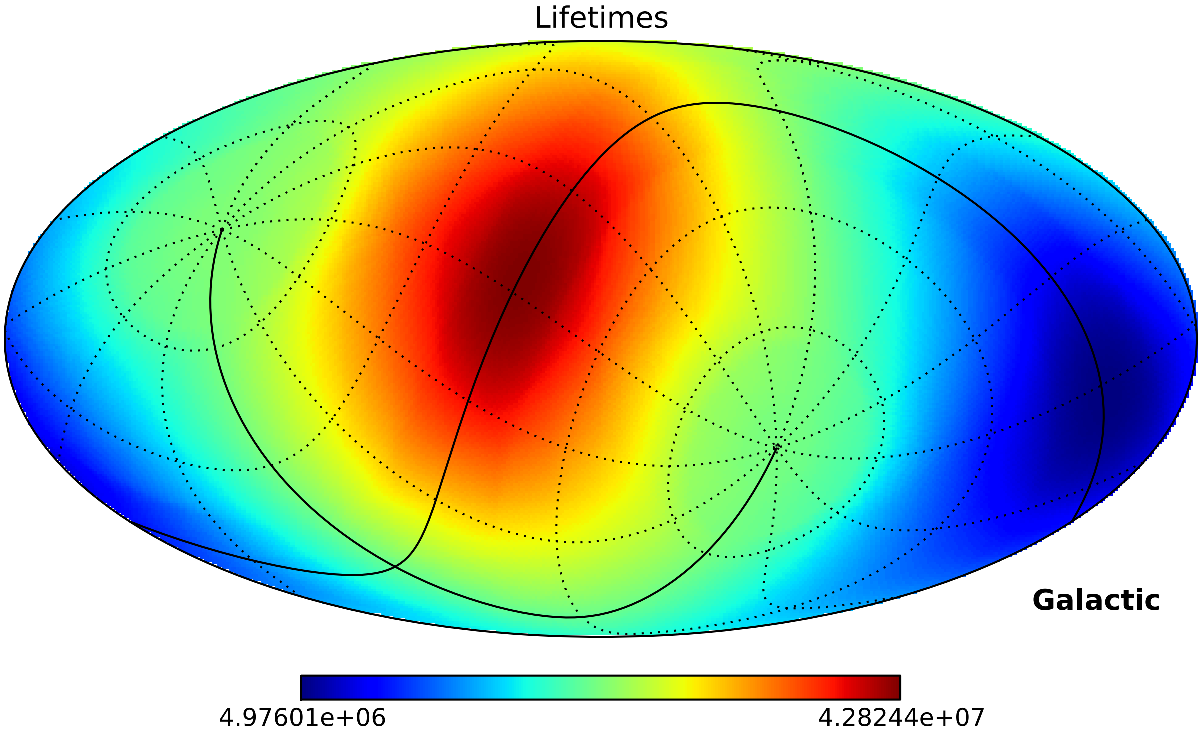

Figure 3.2: Integrated lifetimes in seconds, for the fourth of April 2008 to the 22nd of March, 2013. The grid is celestial coordinates, while the map is in galactic.

Angular Resolution

Multiple scattering degrades the Fermi angular resolution at low energies, while the high-energy photons should be limited by the segmentation in the tracker[6]. However, the simulation may have underestimated the error by a factor of 2, and a conservative limiting resolution is about 0.2° above 20 GeV[5].

Effective Area and Exposure

The effective area for the `P7SOURCE` photons is included with the Fermi Science Tools[1]. It is given as a function of incident angle on the spacecraft, and the log of the energy.

---

[1] `http://fermi.gsfc.nasa.gov/ssc/data/analysis/software/`

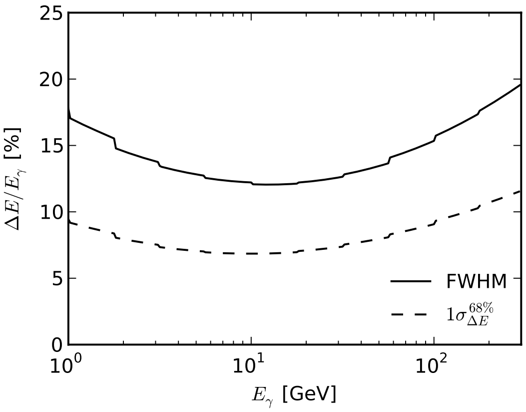

Figure 3.3: Energy resolution and full width at half maximum from[68]

Two different responses are given, according to if the photon pair-converted in the first 12 layers (front), or if it converted in the four thicker layers (back).

The exposure is computed to take the pointing history of Fermi into account; by integrating the effective area given the line of sight $\hat{\boldsymbol{p}}$, and analysis cuts over the observation period:

$$\mathcal{E}(E, \hat{\boldsymbol{p}}) = \int A_{\text{eff}}(E, \hat{\boldsymbol{v}}(\hat{\boldsymbol{p}}, t),) \tag{3.1}$$

Where $\hat{v}(p, t)$ is the line of sight in spacecraft coordinates. The angular resolution is taken into account as well in the Science tools, and results in a diffuse edge to the selected region at lower energies, where some photons originating in the selected region will not be including, and some from the outside will leak in. With larger selected regions, and a smaller uncertainty at higher energies, the exposure becomes sharper.

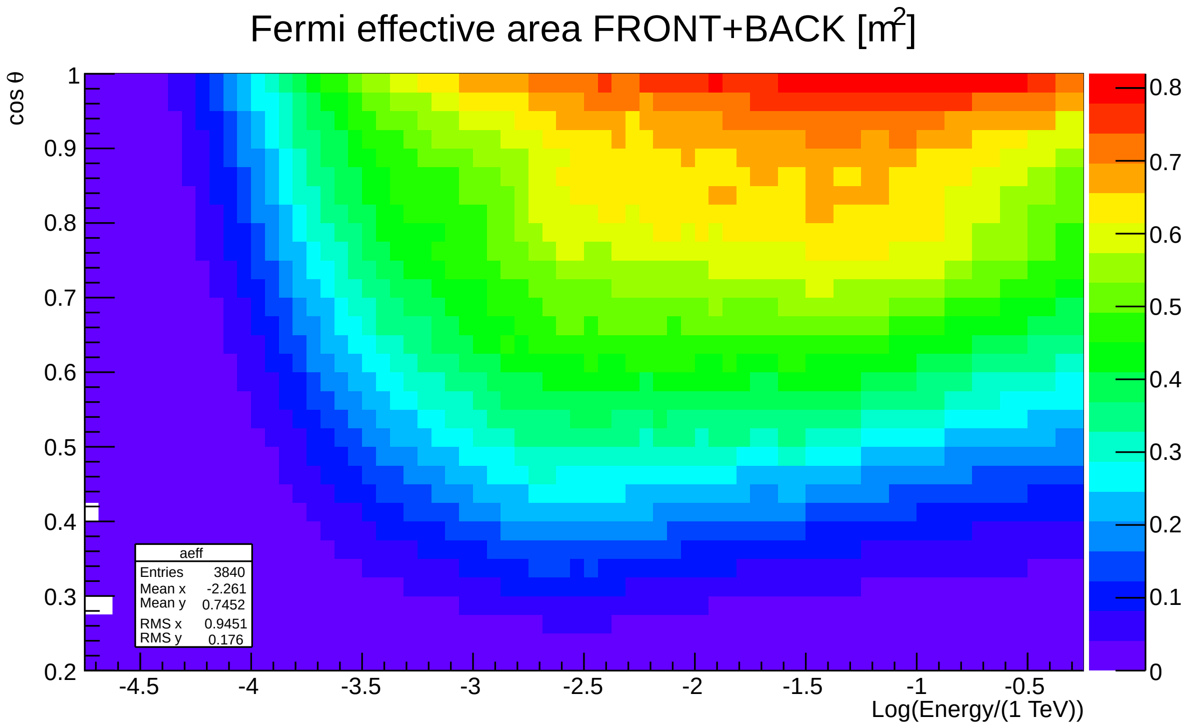

Figure 3.4: The Fermi effective area summed over front- and back-converted photons using the `P7SOURCE` response function. as a function of energy and incident angle

3.2 Dark Matter limits

Fermi-LAT has set limits on dark matter; both on the $\langle \sigma v \rangle_{\gamma\gamma}$ from line searches as above [5], and the total cross-section[4] The latter limits are set assuming that the annihilation goes to a specific pair of standard model particles, so when I read it off I must take care.

3.3 Dark matter

Recently, an apparent signal has been identified in the Fermi data[70]. Using a region optimized for dark matter detection, he found a locally significant result of 4.6σ at 130 GeV. Astrophysical sources will generally not have sharp peaks, so this would be an indication that the feature may be from dark matter. However, a line signal is seen when the LAT is pointing towards the edge of the earth, which would point to a systematic effect[8]. It is not very reasonable, however to expect Fermi-Lat to be able to resolve this on their own. Hess

3.4 The ATLAS experiment

The ATLAS (A Toroidal LHC ApparatuS) detector is one of two multipurpose-detectors at the Large Hadron Collider at CERN.

3.4.1 The LHC accelerator

The LHC is a proton-proton accelerator, 27 km in diameter, designed to accelerate the particles up to 7 TeV. In 2013, the LHC was running at beam energies of 4 TeV, and delivered luminosities of around $6 \times 10^{33}\,\mathrm{cm}^{-2}\,\mathrm{s}^{-1}$[54] to ATLAS.

The maximum center-of mass energy was 8 TeV, however, the energy of the protons must be distributed among the valence quarks, as well as among the sea of virtual gluons and quarks that make up the bulk of the proton rest mass. Therefore, the center of mass of a collision will be boosted with respect to the detector. Therefore, the total longitudinal momentum cannot be measured. The transverse momentum of the collision products, should, on the other hand balance out. In addition to the usual spherical coordinates with z along the beam axis. the pseudorapidity $\eta = -\ln\tan(\theta/2)$, or rapidity $y = 1/2\ln[(E + p_z)/(E - p_z)]$ in the case of massive particles. In the limit, rapidity approaches pseudorapidity at the limit $m \to 0$ In the case that a particle is boosted along the beam axis, differences in rapidity will be invariant, and so differences in rapidity will be stable despite the unknown longitudinal boost.

3.4.2 The structure of ATLAS

ATLAS is 44 m long, and 25 m tall. Two magnetic fields bend charged particles; a 2 T field in the $\hat{z}$ direction, produced by a solenoid 2.5 m in diameter, as well as a vast outer set of magnets that sets up an ≈ 0.5 T toroidal field in the outer detector[25].

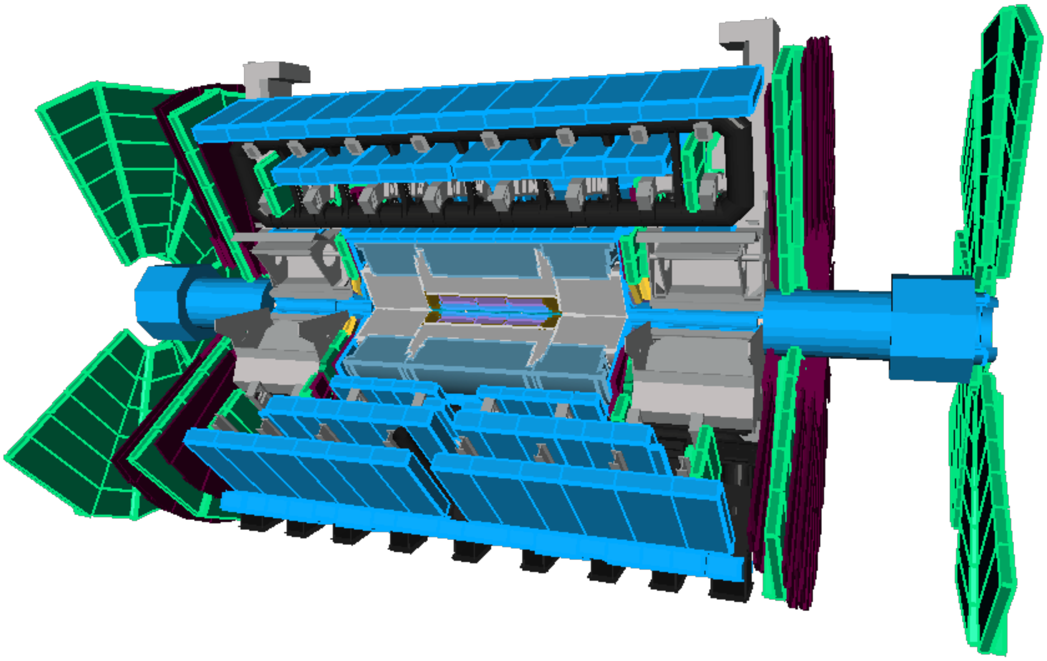

Figure 3.5: The ATLAS detector. Starting from the middle, the inner detector in blue is contained in the transition radiation tracker in purple. The electromagnetic calorimeters in gray, and hadronic in dark blue follow after the thin magnet. Enveloping it all, the muon plates surround the detector, with one of the eight toroidal magnet visible.

Inner Detector

The ATLAS inner detector consists of a vertex detector, made from pixel detectors, as well as silicon microstrips. Outside these two detectors is a transition radiation tracker, consisting of gas-filled tubes that add to the resolving power of the detector. The η coverage is up to ± 2.5, which also is the η we will cut on in the analysis to be certain of having the tracker.

Calorimeters

The ATLAS calorimeters are sampling calorimeters, with lead absorbers and argon gas in the electromagnetic calorimeters, followed by steel and scintillator in the hadronic calorimeters [25].

Muon Systems

The bulk of the detector volume is made up of the muon spectrometer; made up of a 25 times 10 meter toroidal magnet, combined with muon detectors allowing a determination of the muon as it escapes the detector.

3.5 Experiments and bounds

In this section, I will write a small note on each of the limits that I use further on.

3.5.1 LEP

The Large Electron-Positron collider searched for supersymmetry, and produced 95%limits for the mass of supersymmetric particles. Charginos were excluded up to 103.5 GeV, given that the difference in mass between $\tilde{\chi}^{\mp}$and $\tilde{\chi}_1^0$is greater than 3 GeV[52].

The stau mass limit ranges from 87 GeV to 93 GeV[53].

3.5.2 IceCube

The IceCube detector is a neutrino telescope that detects Cherenkov light of muons resulting from neutrino interactions. The sun may capture dark matter if it interacts weakly with ordinary matter, and the captured dark matter may coannihilate. Over sufficient time, an equilibrium will be reached, and the number of dark matter particles annihilating will be equal to the number captured. Searching for excess neutrino fluxes from the sun, possibly arising from dark matter coannihilation may then be directly related to the dark matter capture, that mainly depends on the spin-dependent WIMP-nucleon cross section. The IceCube experiment reports 90% limits down to $1 \times 10^{-39}\,\mathrm{cm}^2$, depending on the WIMP mass [3].

3.5.3 XENON100

The XENON100 experiment searches for dark matter in the recoil of very pure xenon. The collaboration gives 90% limits that reaches $1 \times 10^{-44}\,\mathrm{cm}^2$ at $m_{\mathrm{WIMP}} \sim 40\,\mathrm{GeV}$ [14]. The limit, in addition to results from some previous direct detection experiments are plotted in Figure 3.6. XENON100 robustly excludes the favored regions of the experiments that report one.

3.5.4 CTA

The Cherenkov Telescope Array is a planned array of telescopes of different sizes, that together will provide improved coverage of the energy range; A handful of big, sensitive telescopes for low energies, as well as a number of small telescopes to cope with the big showers at high energy.[21]

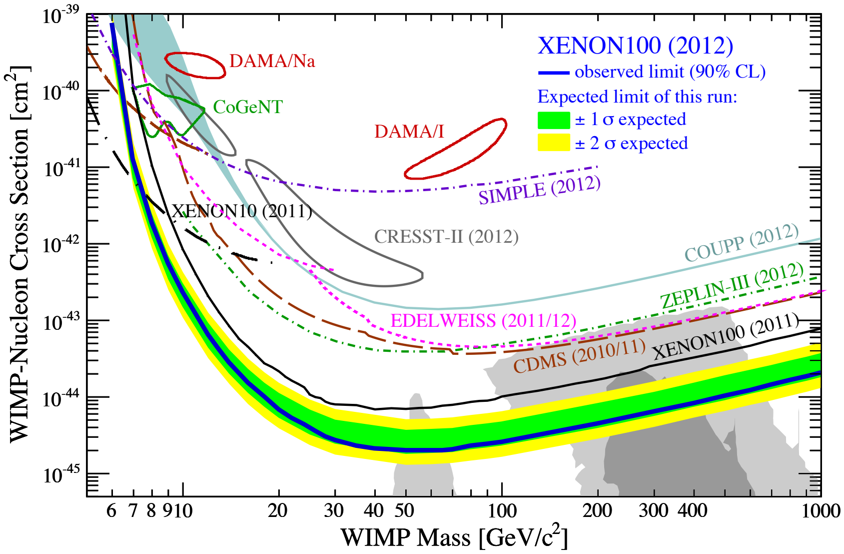

Figure 3.6: XENON100 90% exclusion from [14].

3.5.5 LHCb

The rare decay $B_s \to \mu^-\mu^+$ has been observed at LHCb. They measure a branching ratio $3.2^{+1.5}_{-1.2} \cdot 10^{-1}$[2]. To be within one standard deviation, then, would mean $BR_{1\sigma} < 4.7 \times 10^{-9}$ is the upper limit.

4

Analyses

4.1 Likelihood analysis of Fermi

One of the most convincing signatures of dark matter would be a sharp peak in an otherwise continuous photon spectrum resulting from the annihilation of two dark matter particles. The discovery of a line in the Fermi data around 130 GeV by Weniger [70] has caused great interest in this signature. The local significance of the line was 4.6σ. The discovery of a similar line feature when observing the edge of the Earth, and the ambiguous nature of the time evolution of the significance strengthens the imperative to reproduce the result at another experiment. To support an exploration of the sensitivity of the planned CTA Cherenkov Telescope[26], I have adapted the software used in the analysis to perform a simple maximum likelihood search for a line in the spectrum using the publicly available photon data from the Fermi experiment.

4.1.1 The maximum likelihood method

To estimate parameters of a distribution, the maximum likelihood method is used. As the name suggests; the method searches for the probability distribution that would make it most probable to get the observed data. As with any fit method, the result will be constrained by the function you are fitting. For a fit probability density function $f(\boldsymbol{x}, \boldsymbol{\theta})$, where $\boldsymbol{x}$ is a vector of the measured properties of one data point, and the $\boldsymbol{theta}$s are the parameters being fitted. Assuming that the individual measurements are not correlated, the likelihood $\mathcal{L}$ is the product of the individual probability densities:

$$\mathcal{L}(\boldsymbol{\theta}) = \prod f(\boldsymbol{x}_i, \boldsymbol{\theta}) \tag{4.1}$$

For an easier computation, the logarithm of the likelihood is the quantity one actually maximizes:

$$\log \mathcal{L}(\boldsymbol{\theta}) = \sum \log \left(f(\boldsymbol{x}_i, \boldsymbol{\theta}) \right) \tag{4.2}$$

The ratio between the maximum log likelihood given the signal and null hypothesis will tend to a χ^2-distribution as the number of data points go to infinity[69]:

$$2(\log(\mathcal{L}) \log(\mathcal{L}_0)) = 2 \ln \left[\frac{\max_{\theta \in \theta} \prod_i f(\boldsymbol{x}_i, \boldsymbol{\theta})}{\max_{\theta \in \theta_0} \prod_i f(\boldsymbol{x}_i, \boldsymbol{\theta})} \right] \sim \chi^2(\nu) \tag{4.3}$$

Where the number of degrees of freedom, ν, is the difference in degrees of freedom in the null hypothesis and signal case. The χ^2-distribution may then be used to set limits. For example, a 95% confidence interval is the region where $\log \mathcal{L}(\theta)$ is smaller than $\max \log \mathcal{L}(\theta_0) + \frac{1}{2}\chi^2(nu)_{.95}$. For one degree of freedom, the critical value is $\chi^2(1)_{.95} = 3.841$.

4.1.2 Model of spectrum

The fit function used to model the flux is the sum of a power-law spectrum, representing the usual background of the galactic center[29], and a Gaussian distribution with the width of the detector resolution representing a line spectrum:

$$\Phi_{\text{line}}(E, m) = \Phi_{0\text{line}} e^{-\frac{(E-m)^2}{2\sigma_E^2}} \tag{4.4a}$$

$$\Phi_{\text{background}}(E, \Gamma) = \Phi_{0\text{background}} \left(\frac{E}{1\text{TeV}} \right)^{-\Gamma} \tag{4.4b}$$

The number of photons hitting an area is $n_\gamma(E) = \Phi(E) * A_{eff}(E)$ Both formulas are normalized over the energy range being fitted, and added so that the line spectrum constitutes a fraction α of the total probability density.

$$f_{\mathrm{i}}(E, m, \Gamma, \sigma_E) = \Phi_i \left(\int_{E_{\min}}^{E_{\max}} \Phi_i(E, m, \gamma, \sigma) \mathrm{d}E \right)^{-1} \tag{4.5a}$$

$$f(E, m, \Gamma, \sigma_E, \alpha) = \alpha f_{\mathrm{line}}(E, m, \sigma_E) + (1 - \alpha) f_{\mathrm{background}}(E, \Gamma) \tag{4.5b}$$

4.1.3 Data utilized

The photons used in the analysis were taken in a 20° radius around the galactic center, located at 266.417°,−29.007° in celestial coordinates. This corresponds to the center region of [5] The time period was from the fourth of October 2008 until the eight of May 2013. The photon energy is chosen between 100 MeV and 300 GeV. The variability in effective area at energies below 100 MeV leads to the cut at this energy[34].

Using the Fermi `Science Tools`, I impose standard quality cuts on the lists retrieved from the Fermi photon database[1].

- Photons must meet the `P7SOURCE_V6` quality criteria, as recommended for galactic point and diffuse analyses[34].
- *DATA_QUAL==1, LAT_CONFIG==1* excludes periods of bad data.
- The zenith angle must be less than 100°, to avoid gamma rays from the Earth at 113°.
- Times when Fermi was pointed at a specific source is suppressed by requiring the rock angle < 52.
-

After using `gtselct` to cut on these qualities, `gtmktime` restricts the photons to those occurring in Good Time Intervals, when the instrument was running smoothly, as well

---

[1] The Fermi data, updated continuously, is available at `http://fermi.gsfc.nasa.gov/ssc/data/`.

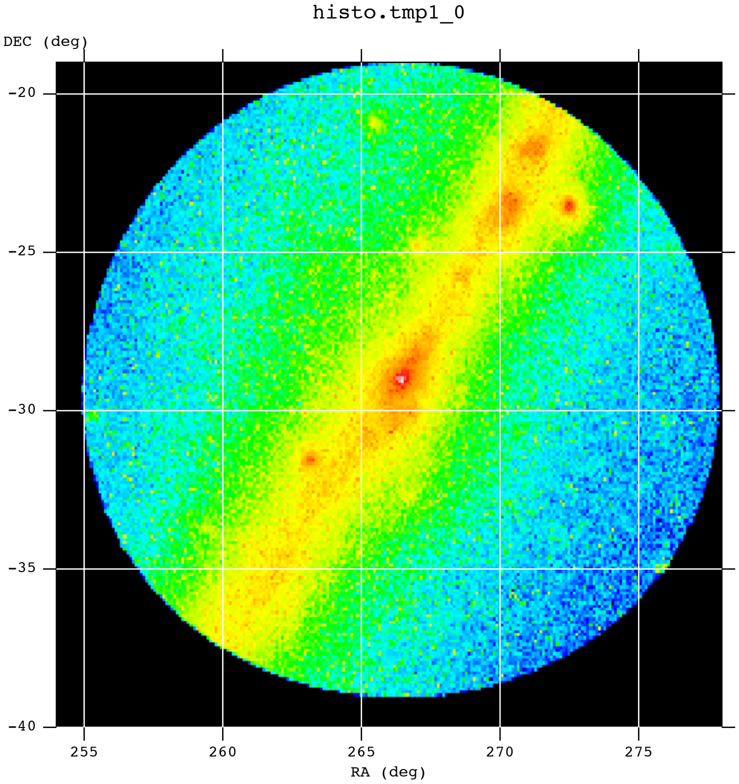

Figure 4.1: The Galactic Center as imaged by Fermi, in celestial coordinates. The image is weighted by energy, and on a logarithmic scale.

as requiring the instrument to have the region of interest in its field of view[30]. The resulting photon file is translated from `.fits` to `.root` and imported into the analysis program using `pyfits`. The `gtltcube` computes the integrated livetime for the selected region, and `gtexpmap` computes the exposure map in the region of interest as a function of energy.

4.1.4 Analysis

The analysis is performed using the `TMinuit`[10] implementation of the `Minuit`[48] optimization algorithms. The likelihood function of the photon collection is fitted to the power law, assuming no signal. The fit is performed in a window that is six times the Fermi energy resolution up and down from a fixed energy. Using the fitted background power, the signal fraction is unfrozen, and a bisection search[2] performed to identify the 95% limit corresponding to a gap in the log likelihood of 3.841.

The search is repeated over the range of masses to probe. For easier comparison with [5], I probe 20 to 200 GeV in 10 GeV increments, as well as 7, 10 and 15 GeV.

When the 95% limit on signal fraction in the window is computed, this correspond to $n_{\gamma\gamma 95\%} = n_{\text{window}}\alpha_{95\%}$, where n_{window} is the number of photons in the mass window.

To translate the limit on excess photons into a cross-section, it is necessary to consider the amount of dark matter you expect to look at.

4.1.5 Limits on Cross-Sections

The flux of photons over the selected region of interest is approximated by $\Phi = n/\bar{\epsilon}$. The variation in exposure over the region of interest $\text{RMS}(\epsilon)$ is below 10% above 1 GeV. Approaching the problem from the other direction; the expected flux is:

$$\Phi = \frac{\langle\rangle}{2\pi m_\chi^2} \int_{\Delta\Omega} \int_{\text{LOS}} \rho^2(r) \mathrm{d}s \tag{4.6}$$

Where the s integral runs over the line of sight, and r is the distance between the volume element and the galactic center. In the case of the Milky Way, the integral runs over $0 < s < 150\,\text{kpc}$ and galactic latitude and longitude from 0° to 20°.

The Dark Matter Distribution

The density distribution of dark matter will affect the computed limit. Many distributions have been proposed to fit the observed rotation curves; in this analysis the Einasto distribution is used[38]:

$$\rho(r) = \rho_s \exp -\frac{2}{\alpha} \left[\left(\frac{r}{r_s}^{\alpha} - 1 \right) \right] \tag{4.7}$$

---

[2] I.e. divide the area in two, assume the function is monotonic and go to the half where it is. Repeat.

With $\alpha = 0.17$ and $r_s = 20\,\mathrm{kpc}$[61]. The density is normalized by requiring a density at the sun $r = r_{\mathrm{sun}}$ of $0.4\,\mathrm{GeV\,cm^{-3}}$.

4.2 Computation of supersymmetric parameters

4.2.1 Program packages used

ISAJET

The ISAJET[63] program package contains ISASUSY routines to compute the masses and decay modes given the mSUGRAparameters at the unification scale:

- the sfermion mass m_0,
- the gaugino mass $m_{1/2}$,
- the trilinear coupling A_0,
- the Higgs vacuum expectation value $\tan\beta$,
- and Higgsino mass sign $\mathrm{sgn}\mu$.

ISASUSY takes these parameters, as well as the top mass, and computes the renormalization group equations. Gauge couplings, Youkawa couplings and soft breaking terms are computed to two loops[63].

In addition to the supersymmetric spectrum, the IsaBSMM routine computes the branching fraction of the flavor changing process $BF(B_s \to \mu^+\mu^-)$. The BF is strongly dependent of $\tan\beta$, [63, p.91].

The LHCb experiment has measured the branching fraction of $B_s \to \mu^+\mu^-$ to $3.2^{+1.5}_{-1.2} \times 10^{-9}$ [2].

DarkSusy

The DarkSusy [41] package computes the properties of neutralino dark matter in the MSSM. It reads the `.slha` mass spectrum from IsaJet to

Since R-parity is assumed to hold, as detailed in section **??**, all supersymmetric particles will decay into the lightest supersymmetric particle. Therefore, to compute the number of stable relics, it suffices to sum up the number of all supersymmetric particles. After the heavier supersymmetric particles have decayed, the relic density n will evolve with the expansion of the universe, scattering off of other particles. In addition, DarkSusy computes thermally averaged cross-sections for LSP-LSP annihilation $< \sigma v >$. The LSP-nucleon cross sections are computed both in spin-dependent and independent versions, to be compared with limits from direct detection.

Lastly, DarkSusy computes the decay $b \to s\gamma$, which, like $B_s \to \mu^+\mu^-$ may be enhanced by new decay diagrams in SUSY[42]. DarkSusy implements a formula due to Misiak et al.[57], and constrains it within $2.71 \times 10^{-4} \geq BR[B \to X_s\gamma] \geq 4.39 \times 10^{-4}$[13].

FeynHiggs and HiggsBounds

In the light of the recent Higgs discovery, it is imperative to include Higgs constraints in SUSY. FeynHiggs provides a dedicated program package to compute the Higgs mass, as well as other properties[39, 35, 46, 45]. This package is compiled together with HiggsBounds, which receives the results from FeynHiggs, and flags models that are excluded at 95%, and prints the Higgs mass. The version used is HiggsBounds `3.8.0` and FeynHiggs `2.9.2`. HiggsBounds `3.8.0` includes results from ATLAS, CMS and Fermilab up to 2012[3][15]

---

[3] The manual contains an exhaustive list

4.2.2 Errors

top mass

ISAJET takes the top mass as input. Some supersymmetric parameters show a strong dependence on the tau mass. The Higgs mass is strongly affected:

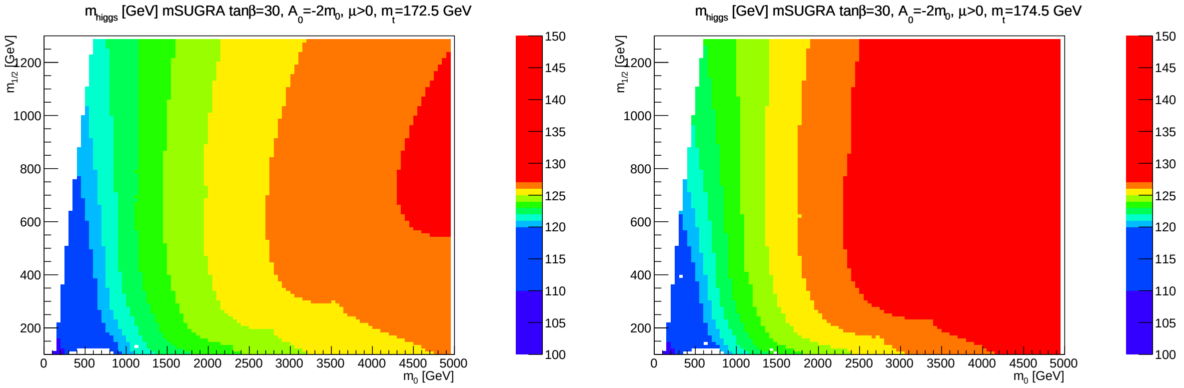

(a) $m_t = 172.5$ GeV (b) $m_t = 174.5$ GeV

Figure 4.2: Higgs masses for the Higgs-aware grid, for two top masses $m_{t\pm} = m_t \pm \sigma_{m_t}$. The m_{top} dependence mentioned in section 2.3.2 is clear.

Higgs masses

The Higgs mass computed by FeynHiggs

4.2.3 Running

I use a python steering script to call Isajet 7.82, DarkSusy 5.0.5 and FeynHiggs 2.9.2 +HiggsBounds 3.8.0 in sequence. The `.slha` file computed by Isajet is input to the other program packages unless a severe error, such as a charged lightest supersymmetric particle or other theoretical inconsistency is reported from IsaJet.

As far as possible, I have attempted to modify the individual program packages into black boxes that may be called by command line arguments without any interaction. Calling these boxes for each run eliminates race conditions between the programs that depend on input from each other, as well as a significantly more robust if one point should crash.

Each program outputs their parameters to a temporary text file, all of which are collated into a `.root NTuple` for easy access.

To check the computations, I compare my results to Profumo[66]. The paper examines grids in m_0, $m_{1/2}$. These correspond to the sparticle masses at unification, and their masses at the weak scale will be roughly proportional to m_0 and $m_{1/2}$. An example is the chargino limit at low $m_{1/2}$ due to imposing the LEP chargino limit. A comparison is included in figure 4.3. In this, and all subsequent limit plots, accelerator constraints will be colored red, while astrophysical constraints will be in blue. Allowed relic densities are plotted in green.

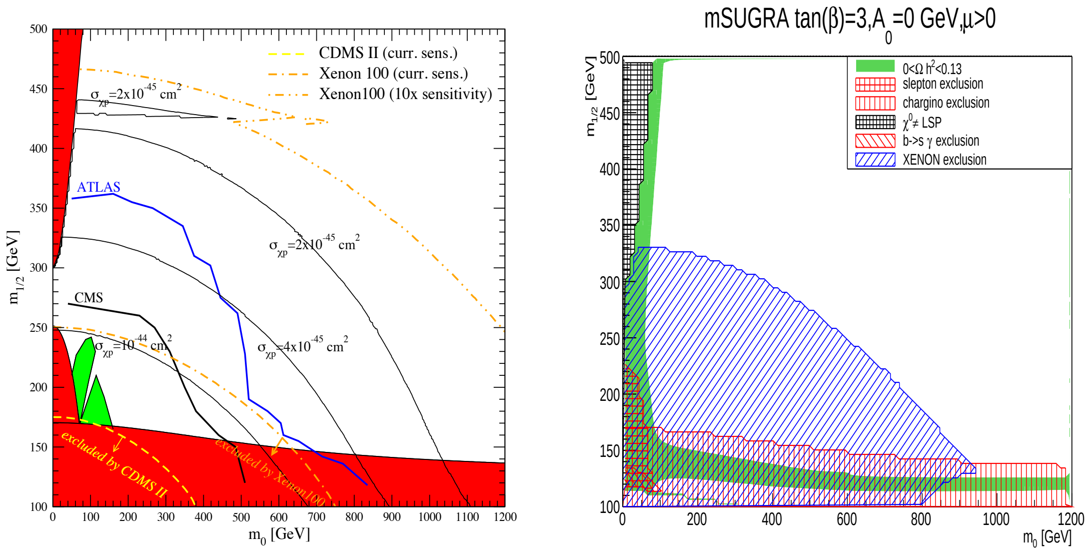

(a) Result from Profumo[66]

(b) My result- including XENON100 exclusion

Figure 4.3: mSUGRAgrids at $\tan\beta = 3, A_0 = 0$ GeV, $\mu > 0$ Note that: -I have not plotted the Tevatron or LHC results, since I am checking my computations, not reproducing every line. -The XENON100 experiment has improved their exclusion greatly since Profumos paper was first written. -and, the relic density plotted on the right agrees with other plots from the paper.

Limits that depend on multiple parameters are included as graphs where points are excluded if they fall above the interpolated line. An example is the spin-independent cross-section for WIMP-nucleon scattering in Figure 4.4.

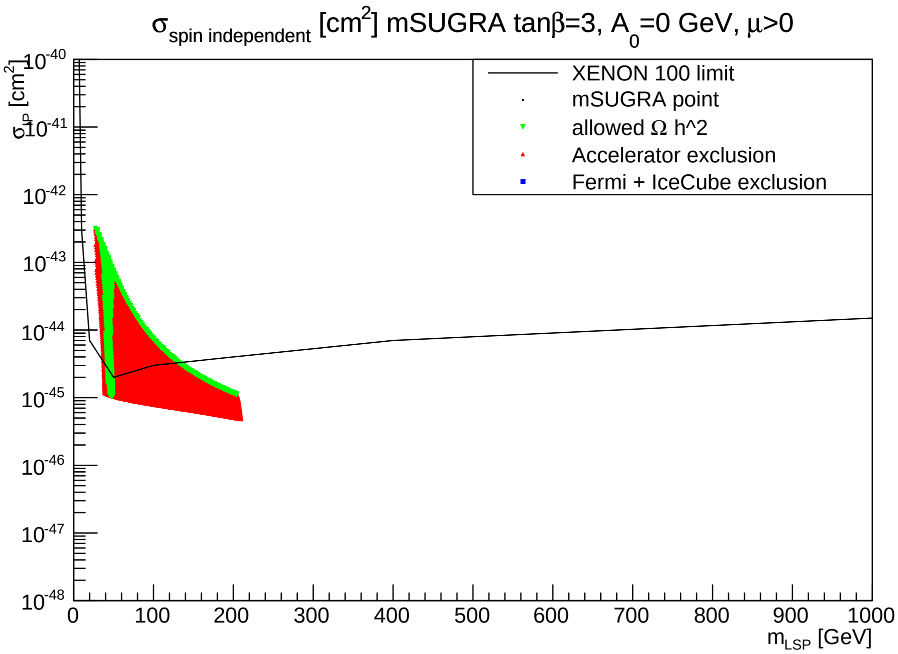

Figure 4.4: The spin-independent cross section as function o neutralino mass for mSUGRA$\tan\beta = 3$

These exclusion limits are read off from text files which in turn were read off from the cited reference.

4.3 A one-tau search for supersymmetry with ATLAS

A search for supersymmetry with hadronically decaying taus was performed with the ATLAS detector[4]. A mSUGRA model was among the models considered. The analysis was able to exclude regions close to the coannihilation region. This is where where the

---

[4] For this analysis, I worked together with others at the particle physics group at the University of Bergen. I will endeavor to talk of the one-τ analysis when I was not chiefly responsible for the work, and use the first person otherwise. Even in the case that I was responsible for an aspect of the analysis, however, I enjoyed help and advice of the others.

stau approaches the neutralino mass, allowing coannihilation in the early universe, and therefore a relic density compatible with measurements.

4.3.1 Definitions

Kinematic variables used in the analysis are: [16]. Note that the definitions of H_T in particular was defined differently for the concurrent $2 - \tau$ analysis.

- η as defined in section 3.4.1.
- $\Delta R = \sqrt{\Delta\phi\Delta\eta}$, the separation between two objects in azimuthal angle and pseudorapidity,
- The transverse scalar sum: $H_T = \sum p_T^{\tau > 20\,\mathrm{GeV}} + \sum p_T^{\mathrm{jet} > 30\,\mathrm{GeV}}$
- The effective mass: $m_{\mathrm{eff}} = H_T + \not{E}_{\mathrm{T}}$
- The smallest azimuthal separation $\Delta\phi_{\mathrm{min}}$
- The transverse mass of the candidate tau and the $\not{E}_{\mathrm{T}}$: $m_T = \sqrt{m_\tau^2 + 2p_T^\tau \not{E}_{\mathrm{T}} \cdot (1 - \cos\Delta\phi(\tau, \not{E}_{\mathrm{T}}))}$

Missing Transverse Energy

A common feature of searches for R-parity conserving SUSY is a stable Lightest Superparticle. In many SUSY models, the LSP is a candidate for dark matter, and so will not interact strongly with matter. Therefore, the typical search for supersymmetry will use the $\not{E}_{\mathrm{T}}$to select events. The missing energy computation used is `MET_Egamma10noTau`, which consists of jets $> 20\,\mathrm{GeV}$, as well as clusters that have not been assigned to a physics object. Jets are calibrated by their energy, and corrections due to other physics objects are applied [16].

Objects

Throughout the analysis, reconstructed physics objects using `SUSYTools 00-02-05` were used. The jets, electrons and muons are subjected to η and p_T cuts. Other cuts for each objects are also imposed, such as the distribution of energy deposits for the jets, a neural network to identify b-jets, and

If two objects overlap, i.e are separated by $\Delta R > 0.2$, this may be one particle or jet that is reconstructed by multiple object chains. If this is the case[16];

- Taus are discarded if they overlap with an e or μ.
- Jets are discarded if they overlap with an e or τ.
- Muons or electrons are rejected when they overlap with jets with a bigger $\Delta R = 0.4$

The tau decays into a W and a ν_τ. The neutrino escapes the detector, adding to the $\not{E}_{\mathrm{T}}$, while the W may produce another neutrino and an electron or muon. Alternatively, the W may produce a quark pair. The one-tau analysis is focused on the hadronic decay of the tau. Thus one avoids one of the neutralinos that would otherwise have been produced by the W. The τ mass is 1776.8 MeV, which allows it to decay into hadrons, such as pions at ~ 139 GeV[22] unlike the lighter leptons. Typical decays are to one or three light mesons[5]. Therefore, tau jets are typically narrow, and a boosted decision tree is used to discriminate the shape of a τ-jet that is seeded from a calorimeter cluster, with the candidate to have a total charge of ± 1.

4.3.2 Backgrounds

The main backgrounds of the analysis are processes that will produce a significant missing energy and a true or fake τ lepton. A W-boson decaying to a tau will give a signal-like signature, while Z production giving fake taus may also contribute.

---

[5] π and K, e.g. $\pi^+\pi^-\pi^-$[22]

To estimate the expected backgrounds, simulated events using the atlasfull simulation are compared with data in control regions that are selected away from the signal region. From there, scaling factors are obtained to normalize the different contributions. The W, t and Z backgrounds are split according to whether they have a true or fake tau, as the relative contribution may change between control and signal regions[16]. The estimate of the background in the signal region is then computed by passing the background Monte Carlo samples through the signal cut chain, and weighting the events with the scaling factor. In effect, one is using the shape of the simulated data while normalizing it to the observed distributions.

W, Z and top

None of the control regions used are completely pure. What you count is the amount of data in each control region, and the amount of each kind of background Monte Carlo that pass your control region cuts.

The result is a matrix that may be solved for the scaling factors given the amount of data and Monte Carlo in the control region. The one tau analysis performs this matrix method on four classes of background:

- W bosons with a true reconstructed tau.
- W and Z bosons with a fake reconstructed tau.
- top with a true reconstructed tau
- top with a fake reconstructed tau

The Z and W fakes were seen to be present in similar levels in the W fake control region, and since the cuts precluded a comparison with $Z \rightarrow \mu\mu$, it was settled to use this scale factor, which the one tau analysis validated at less stringent cuts[16].

The results are reproduced in equation 4.8[16]:

$$\begin{pmatrix} \omega_{W/Z}^{\text{true}} \\ \omega_{W/Z}^{\text{fake}} \\ \omega_{\text{top}}^{\text{true}} \\ \omega_{\text{top}}^{\text{fake}} \end{pmatrix} = \begin{pmatrix} 0.89 \pm 0.03^{\text{stat}} + 0.06^{\text{syst}} \\ 0.66 \pm 0.25^{\text{stat}} + 0.43^{\text{syst}} \\ 0.99 \pm 0.06^{\text{stat}} + 0.07^{\text{syst}} \\ 0.56 \pm 0.79^{\text{stat}} + 0.27^{\text{syst}} \end{pmatrix} . \tag{4.8}$$

The number N_W^{SR} of W background expected in the signal region given by the scale factors and the unscaled number in the signal region $N_W^{\text{MC,SR}}$ is then:

$$N_W^{\text{SR}} = \omega_W^{\text{truth}} N_{W,\text{truth}}^{\text{MC,SR}} + \omega_W^{\text{fake}} N_{W,\text{fake}}^{\text{MC,SR}} \tag{4.9}$$

With an analogous computation for Z and top backgrounds.

QCD

The QCD contribution was estimated using the ABCD-method, in which four signal regions are chosen by changing the cuts made to exclude QCD in the signal region two by two, and then for each pair choose a tau conforming either to the nominal tau cuts, or an extra loose cut. The QCD contribution to the signal region was estimated to $0.03 \pm 0.01^{\text{stat}}$[16].

Diboson

The one tau analysis use the unscaled Monte Carlo in the case of diboson background, as it is seen to be a small contribution, and a significant challenge to obtain scale factors for. The expected number of dibosons in the signal region is $0.12 \pm 0.10^{\text{stat}}$

4.4 Event files

All data used in the analysis were `SUSY` `D3PD`s with the tag `p1328`. The cross-sections are Next to NLO where possible, and NLO otherwise[16].

4.4.1 Simulated data

The simulated data for standard model backgrounds were all computed as part of the `MC12` Monte Carlo effort. The cross-sections used follow the guidance of the `SUSY` working group[11], and

4.4.2 The Higgs Aware grid

The Higgsaware signal grid, with the parameters $\tan\beta = 30$, $A_0 = -2m_0$, $\mu > 0$ was computed using the `ATLAS full` simulation with SOFTSUSY3.6.1 and Herwig++. The UEEE3 and CTEQ parton event and parton model was used. The cross-sections are computed to next-to-leading order in the strong coupling[19, 51, 50, 17, 18]. The cross-sections and uncertainties are constructed the range of multiple sets of computations with different Parton Density Functions and mass scales[49].[6]

The nominal cross section and the uncertainty are taken from an envelope of cross section predictions using different PDF sets and factorization and renormalization scales, as described in Ref. .[7]

The grid has the following parameters:

- m_0 in 200 GeV to 500 GeV steps
- $m_{1/2}$ in 50 GeV steps
- $\tan\beta = 30$

---

[6] These are the recommended references for the ATLAScross-sections, as detailed in [67]

[7] The ATLASTwiki overview of the cross-sections

- $A_0 = -2m_0$
- $\mu > 0$

Table B.1 lists the Higgs aware points at $m_0 \leq 2000$ GeV.

4.4.3 2012 Data

The data used in the analysis are proton-proton collisions, with a center-of mass energy $\sqrt{s} = 8\,\mathrm{TeV}$ which were recorded from April to December 2012, with runs A through L, excluding F and K [16]. The periods which were free from detector issues, such as malfunctioning subsystems, are recorded on the Good Run Lists (GRL), and make up an integrated luminosity of $20.7\,\mathrm{fb}^{-1}$.

4.4.4 Event selection

Trigger

The huge amounts of data generated by ATLASis filtered by triggers that pick signatures of interest. In the 1-tau analysis, the `EF_j80_a4tchad_xe100_tclcw_veryloose` must have been activated, i.e at the minimum a jet with $p_t > 80$ GeV, and $\not{E}_{\mathrm{T}} > 100$ GeV.

After the trigger,quality cuts are applied[16]:

- If the event is from real data, it must be part of the Good Run List.
- The trigger is required to have fired for data
- A primary vertex with minimum five track is required
- No calorimeter noise flag was set
- No cosmic muon candidate or badly reconstructed muon

When the quality cuts have been applied, more cuts are imposed to make sure no events are in regions where the trigger efficiency has not yet plateaued:

- At least two jets with $p_{t1} > 130$ GeV and $p_{t1} > 30$ GeV
- $\not{E}_{\mathrm{T}} > 150$ GeV

The one-tau analysis rejects any events with muons or electrons, and requires exactly one reconstructed τ with $p_t > 30$ GeV. This was found to be effective at reducing the Z background compared to a cut on 20 GeV. If a second tau with $p_t > 20$ GeV is present, the event is rejected to preserve orthogonality to the 2-tau analysis.

QCD

To discriminate against QCD, the azimuthal separation $\Delta\phi_{\mathrm{min}}$ between $\not{E}_{\mathrm{T}}$and the closest jet must be $>$ .3 This will help to exclude instances where $\not{E}_{\mathrm{T}}$is the result of a badly measured jet. In addition, $\not{E}_{\mathrm{T}}/m_{\mathrm{eff}} > 0.3$ is required. Note that m_{eff} will only use the two leading jet.

4.4.5 Other Cuts

The penultimate cut is $m_t > 140$ GeV, which will reject W[16]. In the end the analysis cuts $H_T > 800$ GeV. This will exclude a lot of background, for a detailed discussion of why 800 GeV was chosen, refer to section 4.6.1. The separation between signal and background is evident in Figure 4.8.

4.5 Computing the expected number of events

When the events have been selected, it is necessary for me to weigh them according to the cross-section and number of events that are chosen. The signal file contains events that have been produced in different processes, such as squark-squark, gluino-gluino &c. The events in the

The solution is to count and weigh each sub-process p individually and sum them up at the end, denoting the index of each Monte Carlo event with i:

$$n_{\text{expect}} = \sum_{\text{p}} \sum_{i} \mathcal{L} \cdot \sigma_p \cdot \frac{N_{i,p}^{\text{passed}}}{N_{i,p}^{\text{total}}} \cdot P(\mu_i) \tag{4.10}$$

Where $P(\mu_i)$ is a factor reweighting the event according to the pileup, as detailed in section 4.5, $\mathcal{L}$ is the integrated luminosity, the σ_p is the sub-process cross section as taken from the `SignalUncertainties` file, and the N are the number of Monte Carlo events either passing the cuts or present in the original $D3PD$.

It is clear that is you wish to have the weight of each event, you will need to check the total number of events before you can weigh the Monte Carlo events[8] This is not appropriate if I wishes to save plots etc. along the cutflow, and not solely at the end.

To solve this problem, as well as the prohibitively large file size of the total 219 points of the Higgs aware grid, I decided to first skim the files on the grid, selecting events with $m_T > 50$ GeV and one medium tau with $p_t > 20$ GeV. During this skim, all events are recorded in a map that is used in the subsequent run. Removing the summation signs from equation 4.10, and using the skim data for the N_p^{total}s, I can fill histograms with individual weights.

Pileup corrections

In the ATLASdetector, each crossing of two beam bunches will, on average, result in multiple interactions. When the data was taken, the average number of pileup events was around 20[54]. The simulated background and signal samples are generated with pileup events in a distribution to roughly match the expected conditions. In the analysis, events are reweighted based on the amount of pileup in each events

---

[8] When I talk about a Monte Carlo event, this will refer to a single simulated event at ATLAS, independent of any reweighting.

so that the pileup-distribution matches the empirical distribution. In the analysis, the `PileupReweighting` tool was used to obtain these weights[65][16].

4.6 Errors

The weight of a single event is equation 4.12. The statistical uncertainty is $\sqrt{\sum_i w_i^2}$. The special case where all the weights are the same is obvious. The theory error is straightforward to compute, and is included in Equation 4.12:

$$w_i = \mathcal{L} \cdot \sigma_{p(i)} \cdot \frac{N^{\text{passed}}_{i,p(i)}}{N^{\text{total}}_{i,p(i)}} \cdot P(\mu_i) \tag{4.11}$$

$$\Delta(n_{\text{expect}})_{\text{Theory}} = \sqrt{\sum_{\text{p}} \left(\frac{\Delta\sigma_p}{\sigma_p} \sum_i w_{i,p(i)} \cdot P(\mu_i) \right)^2} \tag{4.12}$$

Where, to avoid confusion the standard deviations are termed Δ.

In addition to statistical errors, and the errors due to uncertainties on the signal cross sections, both of which I compute per process from equation 4.10,systematic effects need to be taken into account. For example; the reconstructed energy in the calorimeters for jets and taus are subject to systematic errors. Another is if the amount of pileup in the detector is systematically over- or under-estimated, then all simulated events would gain a new weight to match the data.

To compute the systematic effects, the program loops over each point for each systematic variation as well as the central value. Taus that would have passed but do not when the tau energy scale is shifted, etc. shift the expected value, and gives a measure of the size of the potential systematic error.

4.6.1 H_T cut

The cut on H_T is the last cut made in the analysis. To choose an appropriate cut value, it is necessary to study the relative amount of signal and background that will pass the cut. It is important to note that this is done entirely with Monte Carlo and scaling factors; the analysis was blinded for $H_T > 600\,\text{GeV}$ before the cut on H_T was chosen.

The experiment is a counting experiment, and the number of events observed will follow a Poisson distribution. The Asimov significance offers a measure of the median significance for this data. This provides a better agreement than the usual $s/\sqrt{b}$ when signal and background is of the same magnitude[33]:

$$z_A \equiv \sqrt{2\left[\left(N_{\text{Sig}} + N_{\text{BG}}\right)\ln\left(1 + \frac{N_{\text{Sig}}}{N_{\text{BG}}}\right) - N_{\text{Sig}}\right]},$$

where the signal N_{Sig} is one of the benchmark points used for optimization and the background N_{BG} is the sum of all SM backgrounds, expected for 20.7fb^{-1} of data.

If the expected number of background events have a significant uncertainty, this must also be taken into account for the expected significance. This calls for a modified Asimov significance, with the background uncertainty $\sigma_{N_{\text{BG}}}$[32]:

$$x_A \equiv \sqrt{2\left\{(N_{\text{Sig}} + N_{\text{BG}}) ln\left[\frac{(N_{\text{Sig}} + N_{\text{BG}})(N_{\text{BG}} + \sigma^2_{N_{\text{BG}}})}{N^2_{\text{BG}} + (N_{\text{Sig}} + N_{\text{BG}})\sigma^2_{N_{\text{BG}}}}\right] - \frac{N^2_{\text{BG}}}{\sigma^2_{N_{\text{BG}}}} ln\left[1 + \frac{N_{\text{Sig}}\sigma^2_{N_{\text{BG}}}}{N_{\text{BG}}(N_{\text{BG}} + \sigma^2_{N_{\text{BG}}})}\right]\right\}}$$

To compute this parameter, I save a histogram in H_T of the weighed events before the ultimate cut for the signal and the different backgrounds. I scale each background according to the scale factors, and integrate the distribution from $H_{T\text{cut}}$ upwards. In addition to the statistical uncertainty of the background histogram, I add the statistical uncertainty given for the scale factor, as well as a conservative 20% systematic uncertainty. The resulting graph, figure **??**, plotted for two signal grid points for the higgsaware grid, as well as two points from the GMSB signal grid.

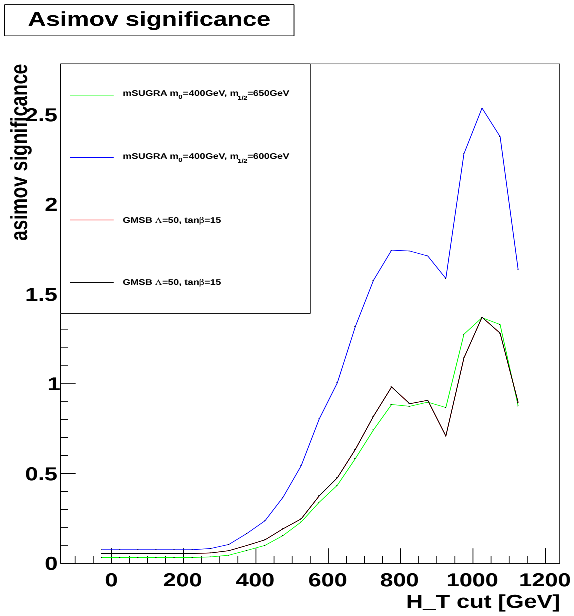

Figure 4.5: The Asimov approximation, including the background and its uncertainties from the one tau analysis, of the signal significance of the GMSB point $\Lambda = 50$, $\tan\beta = 15$ as well as those for the mSUGRA signal points $m_0 = 400\,\text{GeV}, m_{1/2} = 600\,\text{GeV}$ and $m_0 = 400\,\text{GeV}, m_{1/2} = 650\,\text{GeV}$.

4.6.2 Expectations

The figures 4.6 to 4.8 display the agreement between the scaled background and the data for the m_T, the tau transverse momentum and the H_T. Note that the plots in general are filled before the cut on the variable is imposed, with the exception of p_T. The separation in H_T between signal and background is very good.

Predicted background

After running the analysis script over the backgrounds, and scaling them with the various scale factors, I produce the following cut-flow in Table 4.1. Note that the QCD is completely cut away in the cut-flow, but is estimated with another method.

Including systematics, Table **??** displays the full expected background, including statistical and systematic errors:

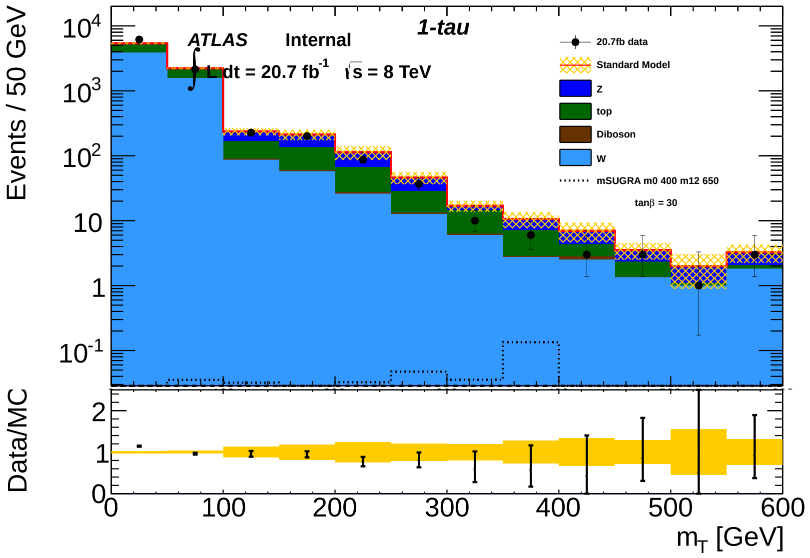

Figure 4.6: m_T for signal, background and data

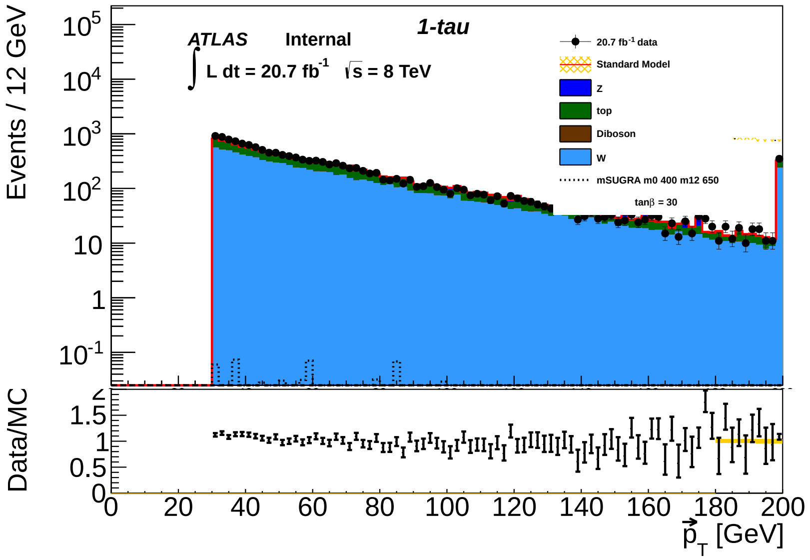

Figure 4.7: $p_{T\tau}$ for signal, background and data

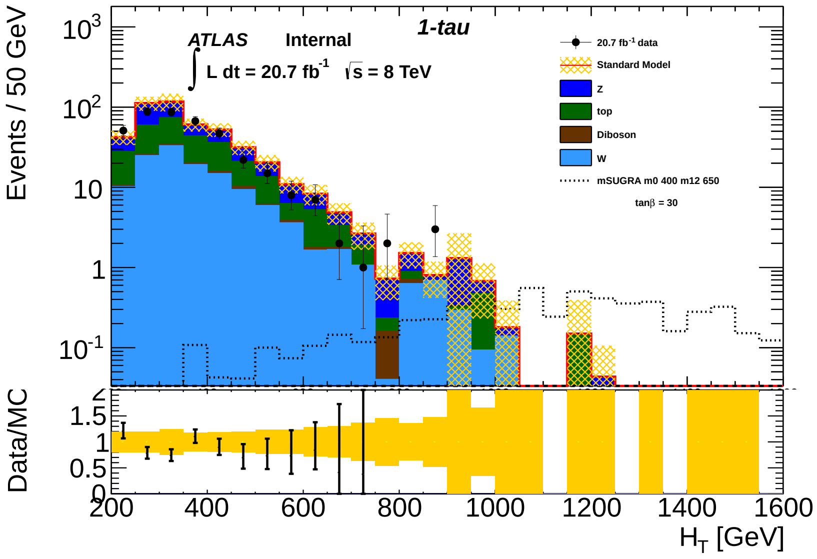

Figure 4.8: H_T for signal, background and data

The Higgs Aware grid

In addition to expected background,

After cut	Top	W+jets	Z+jets	Di-boson	QCD
1τ & no other lepton	5522±751	11601±436	1670±399	59.8±2.2	320±43
$\Delta\Phi_{\mathrm{min}} > 0.3$	3847±367	7923±260	837±163	42.1±1.8	32±12
$\not{E}_{\mathrm{T}}/m_{eff} > 0.3$	2067±209	5613±186	574±138	28.1±1.4	–
$m_T > 140$ GeV	163±106	128±32	173±68	6.5±0.6	–
$H_T > 800$ GeV	0.75±0.58	1.85±0.58	2.1±1.3	0.12±0.10	$0.03 \pm 0.01^{\mathrm{stat}}$

Table 4.1: Cut-flow for the kinematic cuts defining the SR after the baseline event selection. All numbers are from MC scaled to an expected data luminosity of 20.7fb^{-1}with scale factors applied to top, W+jets and Z+jets, except for the final estimate of QCD events. The errors are statistical only.

top (truth)	$0.47 \pm 0.39^{\mathrm{stat}} 0.19^{\mathrm{syst}}$
top (fake)	$0.27 \pm 0.43^{\mathrm{stat}} 0.25^{\mathrm{syst}}$
W+jets (truth)	$1.19 \pm 0.43^{\mathrm{stat}} \pm 0.29^{\mathrm{syst}}$
W+jets (fake)	$0.67 \pm 0.38^{\mathrm{stat}} \pm 0.59^{\mathrm{syst}}$
Z+jets	$2.1 \pm 1.2^{\mathrm{stat}} \pm 1.7^{\mathrm{syst}}$
QCD	$0.03 \pm 0.01^{\mathrm{stat}} \pm 0.02^{\mathrm{syst}}$
Diboson	$0.12 \pm 0.10^{\mathrm{stat}} \pm 0.08^{\mathrm{syst}}$
Total	$4.8 \pm 1.5^{\mathrm{stat}} \pm 1.8^{\mathrm{syst}}$

Table 4.2: Number of expected events at $20.7\mathrm{fb}^{-1}$ that are expected to pass the analysis cuts.

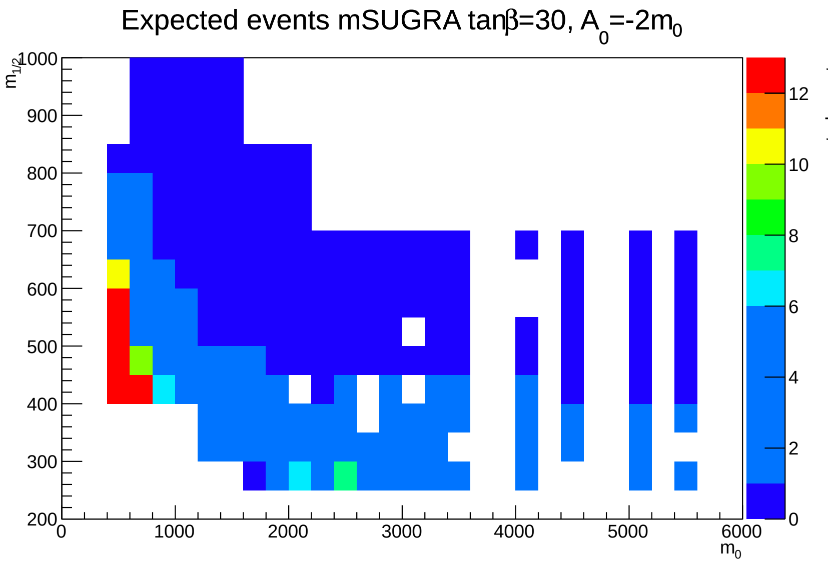

Figure 4.9: Expected number of events passing

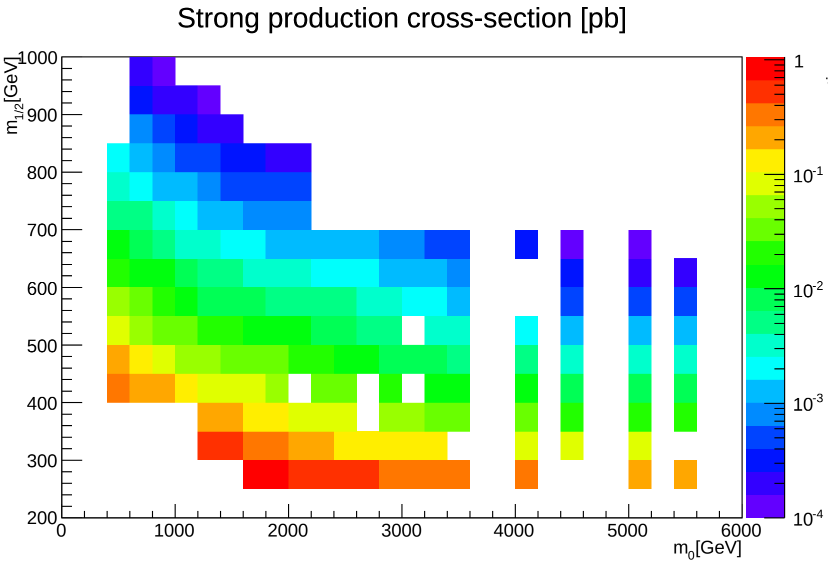

Figure 4.10: The total cross section of the Higgs aware grid points. It decreases monotonically towards higher $m_{1/2}$. Comparing this result to Figure 4.2, one sees that the fraction of events that pass the analysis is a lot bigger in the coannihilation region.

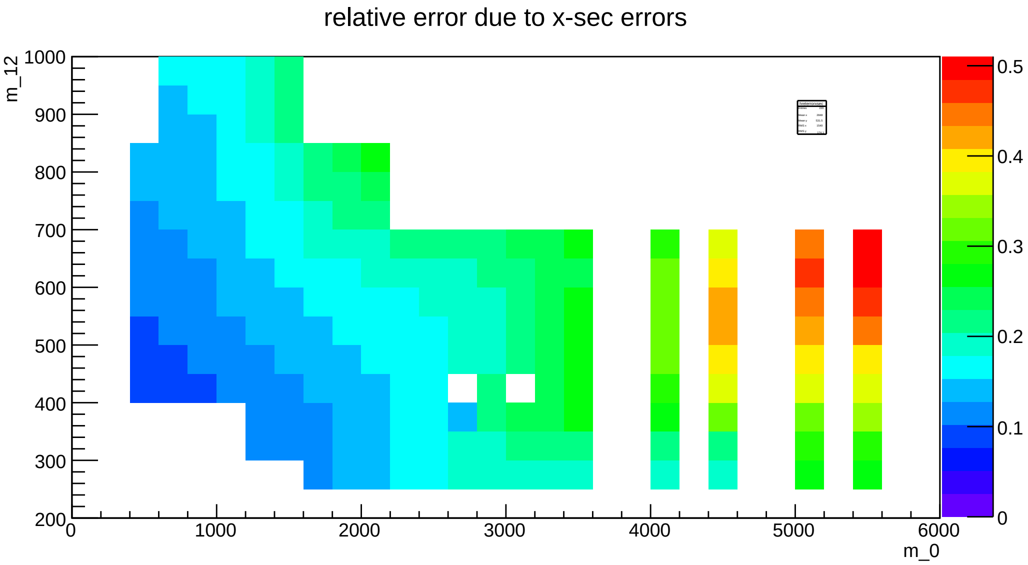

Figure 4.11: The uncertainty of the Higgs-aware cross section. In the region where we expect events, the uncertainty is around 10%

5

Results

5.1 Fermi

The excluded cross section of the line search is included in figure 5.1. A significant less powerful limit is seen at 130 GeV, in line with[70]. A measure of the significance of the line is $z = \sqrt{2(\log \mathcal{L}_{\mathrm{s+b}} - \log \mathcal{L}_{\mathrm{b}})}$. z^2 is included in Figure 5.2. At 130 GeV, $z = 2.51$. In addition, a strong deviation is seen at 7 GeV with $z \sim 3$.

The two most significant features at 7 and 130 GeV have been seen in Fermi analyses of the galactic center, [8]. It is clear that the optimized signal regions used in the papers that found the line is important to achieve a higher significance. However, I see that my linesearch reproduces the result with quite good fidelity, if not with the same high numerical confidence.

The fit to $m = 130$ is displayed in Figure 5.3. It

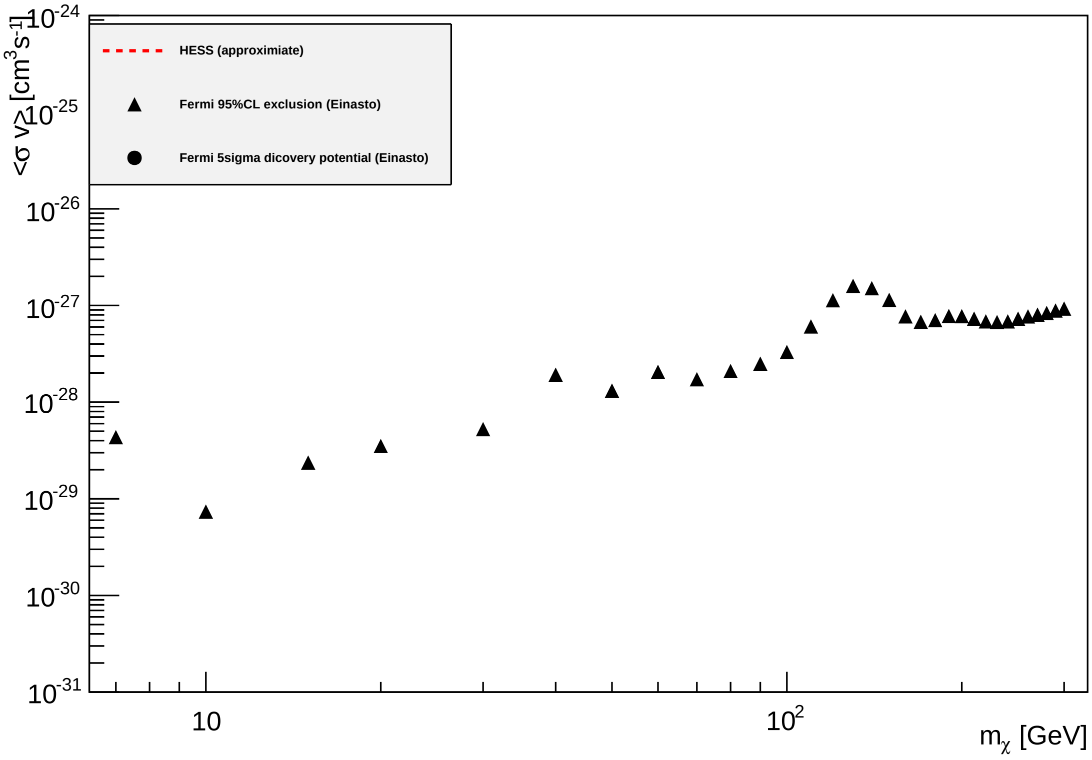

Figure 5.1: The 95% confidence limit for a line signal

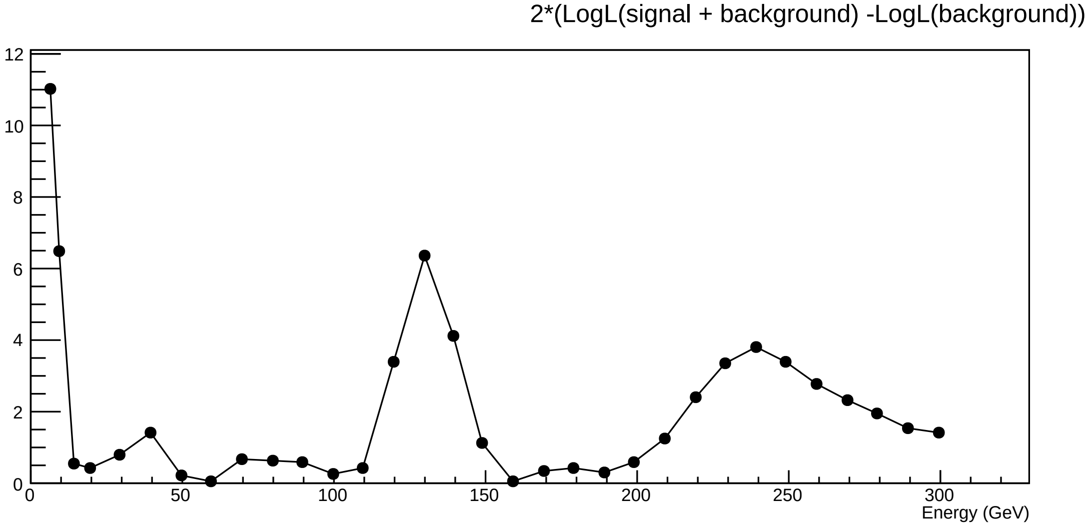

Figure 5.2: $2(\log \mathcal{L}_{\mathrm{s+b}} - \log \mathcal{L}_{\mathrm{b}})$ for the tested masses.

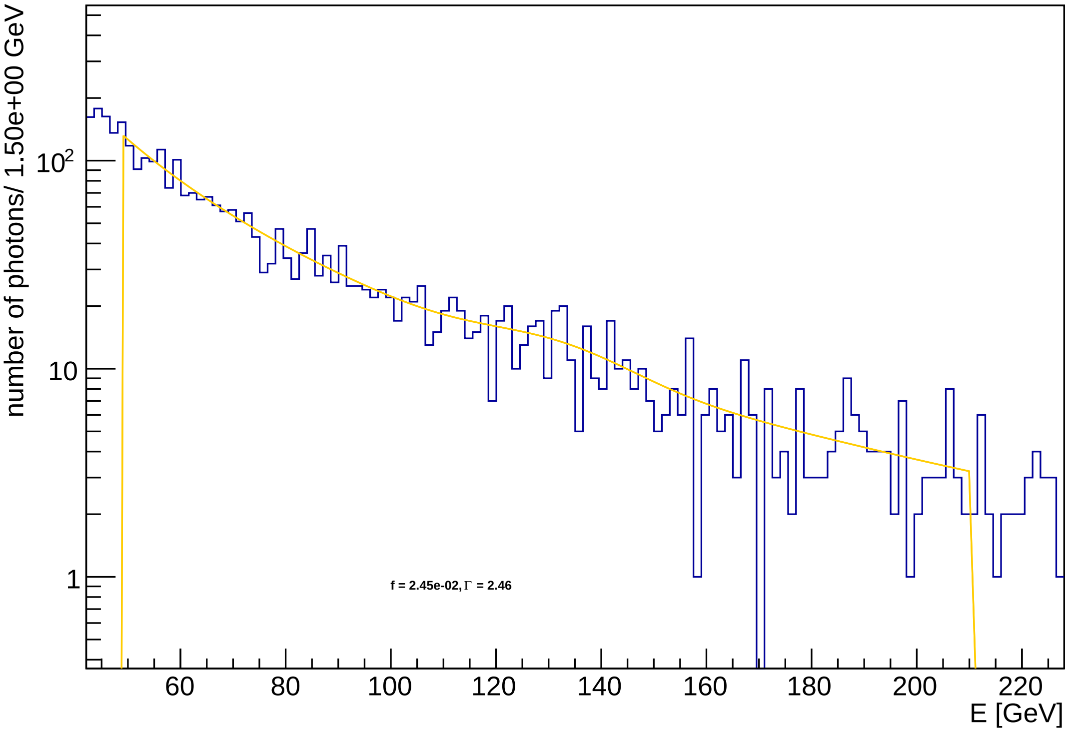

Figure 5.3: The best fit of the model to data at $m = 130$ GeV, with $\Gamma = 2.460 \pm 0.064$ and $f = (2.44 \pm 0.99) \times 10^{-2}$

5.2 Results of mSUGRA computations

5.2.1 Slices of the mSUGRA parameter space

$\tan\beta = 3 A_0 = 0\,\text{GeV}$

The low $\tan\beta$ grids are subject to strong limits, both from XENON100, as is seen in Figure 5.4. ATLAS and CMS have provided strong limits in this case.In addition, the mass of the lightest Higgs boson in this grid only reaches 110 GeV, and is therefore excluded by the LEP results.

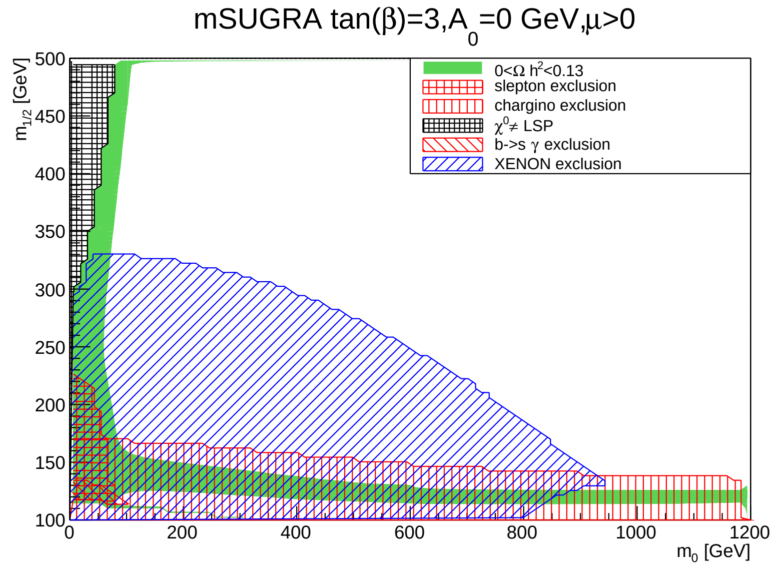

Figure 5.4: A mSUGRA slice at $\tan\beta = 3$, $A_0 = 0\,\text{GeV}$

$\tan\beta = 10 A_0 = 0\,\text{GeV}$

As the ratio of Higgs expectation values increase, the exclusion limits change. Like the $\tan\beta = 3$ case, the $\tan\beta = 10$ slice in Figure 5.5 has a Higgs mass that ranges too low. The maximum is around $m_H \sim 120\,\text{GeV}$.

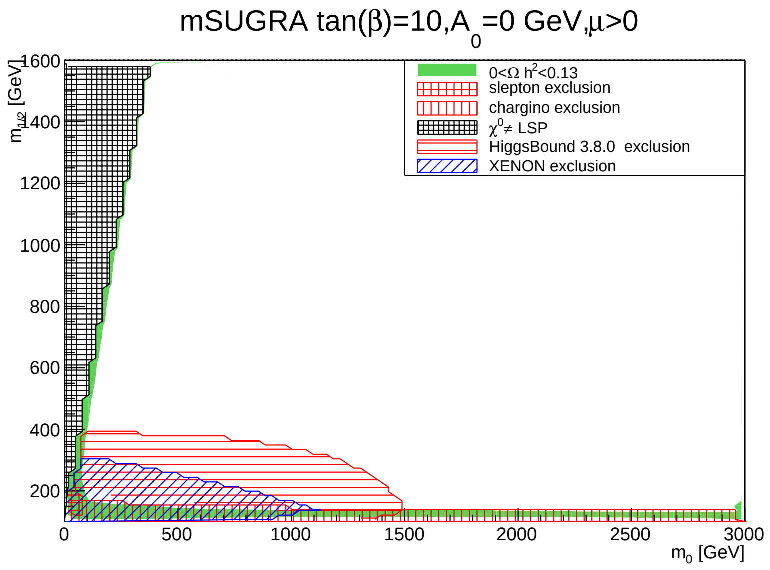

Figure 5.5: A mSUGRA slice at $\tan\beta = 10$, $A_0 = 0$ GeV

$\tan\beta = 40 A_0 = 0$ GeV

The b-physics exclusions on $Br(B_s \to \mu^+\mu^-)$ and $BR(b \to s\gamma)$ are much stronger at higher $\tan\beta$. In the case of $B_s \to \mu^+\mu^-$, there are Feynman loops $\propto (\tan\beta)^6$ [22, p. 1430]. Figure 5.6 suggest comparative advantages of accelerators and astrophysical constraints; while accelerators will in general probe the lower-mass quadrant in the parameter space, astrophysical constraints will reach along regions of higher dark matter cross sections, such as along the hyperbolic branch, which is the region of allowed relic density at high m_0. In this region, the neutralino has a large higgsino component, and the annihilation to Higgs or gauge bosons is enhanced[37]. It can be seen that CTA would be able to exclude dark matter in this region due to the large annihilation cross-section.

$\tan\beta = 30 A_0 = -2300$ GeV

The discovery of a Higgs boson imposed a new constraint on the slices. Above, all slices had too low Higgs masses. A scan made by Burgess et al.[27] highlighted regions of m_0, $m_{1/2}$ around 500 GeV, $\tan\beta \sim 30$, and $A_0 \sim -2300$ GeV with allowed relic densities and Higgs masses. A slice with these A_0, $\tan\beta$ values in Figure 5.7. The Higgs mass reaches

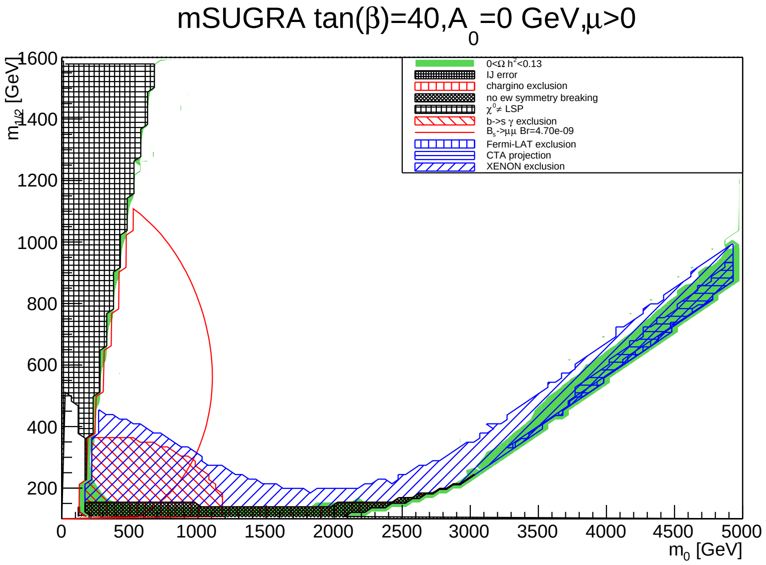

Figure 5.6: A mSUGRA slice at $\tan\beta = 40$, $A_0 = 0$ GeV

125 GeV in the coannihilation region around $m_{1/2} = 800$ GeV.

5.2.2 $\tan\beta = 30 A_0 = -2m_0$

Another slice that contains viable Higgs-masses has been used in ATLAS analyses, particularly in the one-tau analysis that I participated in. Therefore, I will describe the properties of this grid in more detail. The grid of points used in ATLAS, nicknamed the Higgs-aware grid was constructed to maximize the stop-mixing**??**. In addition, the grid features regions of allowed relic density.

A Higgs mass upper bound given in Equation 2.1. The bound may be increased in two ways; either the M_S term may be big,, and the stop correspondingly heavy, or the stop mixing, given by $X_t = A_t - \mu\cot\beta \sim \sqrt{6}M_S$ may give the necessary contribution[36]. The stop mass, like other sfermions, are roughly proportional to m_0, and the top trilinear coupling A_t to A_0. A broad region of acceptable Higgs masses is plain to see in Figure 5.8. As mentioned in section 4.2.2, the uncertainty in the top mass will shift this band in m_0, but the near maximal stop mixing clearly shifts the Higgs mass upwards.

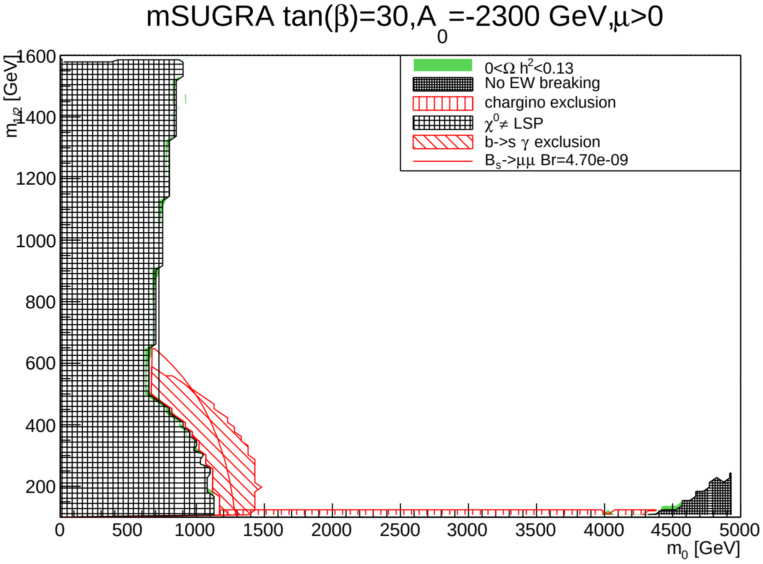

Figure 5.7: A mSUGRA slice at tan $\beta = 3$,

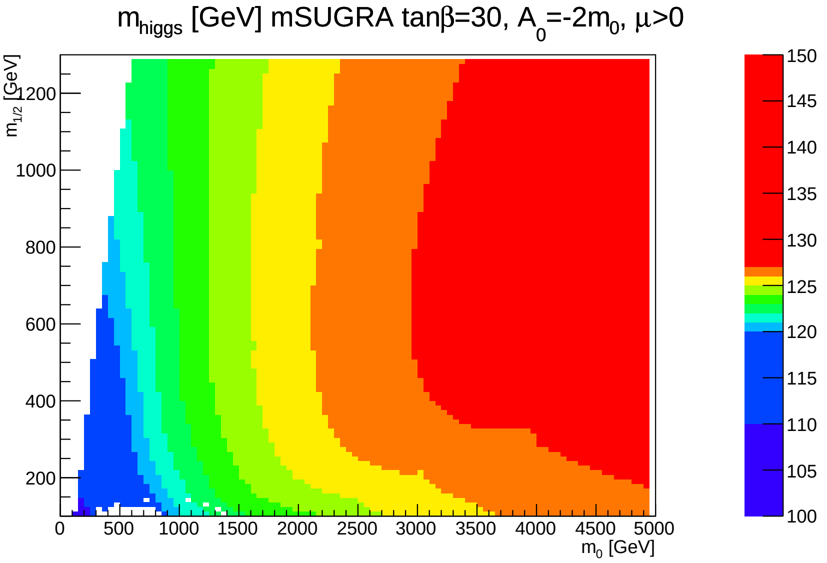

Figure 5.8: Higgs masses in the mSUGRA Higgs-aware grid.

Accelerator bounds

The neutralino and stau masses are plotted in Figure 5.9. The low mass of the stau in the coannihilation region is accompanied by an enhanced stau pair production cross section, and branching ratio of charginos to staus[56]. As the stau is close to the coannihilation region it is the Next to Lightest Supersymmetric Particle (NLSP), and so any staus must decay to a neutralino and a tau . This favors an accelerator search that takes taus into account, such as the one tau search that will be detailed in the next section.

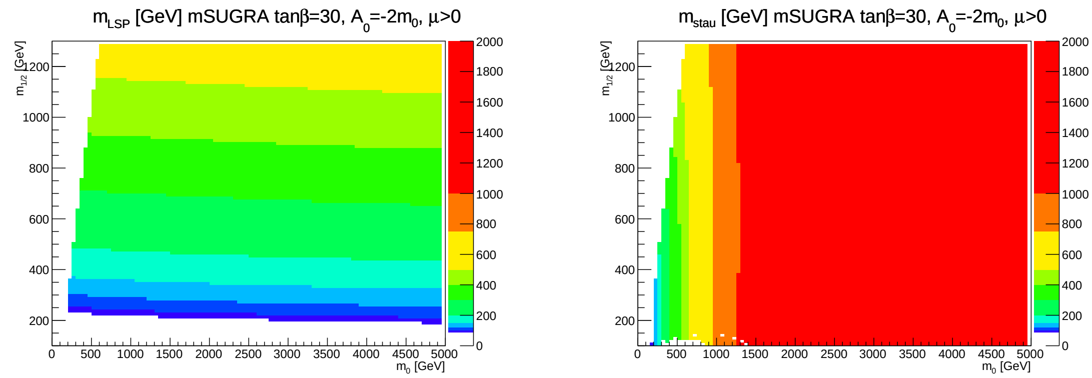

(a) Neutralino

(b) Stau

Figure 5.9: Stau and neutralino masses in the Higgs-aware slice

The branching fraction $B_s \to \mu^+\mu^-$ is enhanced by $\tan\beta$, and is higher than the LHCb central value in the grid. The red area in Figure 5.10 is farther than 1σ from the central value. The 95% confidence limit $BR > 6.2 \times 10^{-9}$ is highlighted in black.

Astrophysical bounds

The relic density of the Higgs-aware grid follows the same pattern as the other slices; a large region of excessive relic density and a sliver along the coannihilation region where the neutralino and stau may coannihilate, reducing the relic density to physical levels.

The astrophysical experiments do not exclude significant portions of the grid, although if the sensitivities were increased, the searches for a photon-photon line would be relevant in the coannihilation region. If the dark matter is lumpy, the ρ^2 dependence would drive

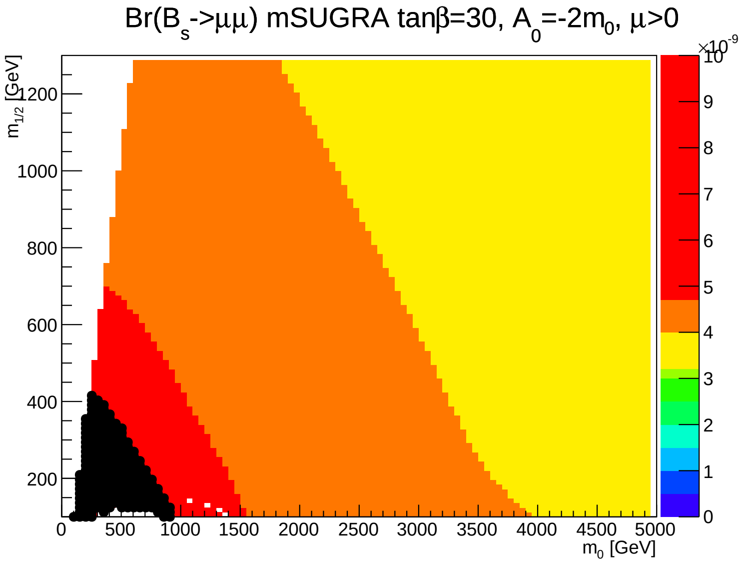

Figure 5.10: The branching ratio $B_s \to \mu^+\mu^-$ as computed by IsaJet.

the exclusion downwards and possibly exclude models through the total $\langle \sigma v \rangle$. This boost factor is not necessarily very high, however[9].

Summary

The Higgs-aware slice demonstrates that for the time being, there are viable Higgs masses in mSUGRA. Beyond that, the coannihilation region stands out as an interesting region for physics; the coannihilation cross sections are the largest here, and a tau-based analysis looks to have some promise. The summary Figure 5.16 shows the grid of points used in the atlas analysis, as well as the B-physics constraints on the lower left part of the slice. 5.17 displays the region of allowed relic density at a higher resolution.

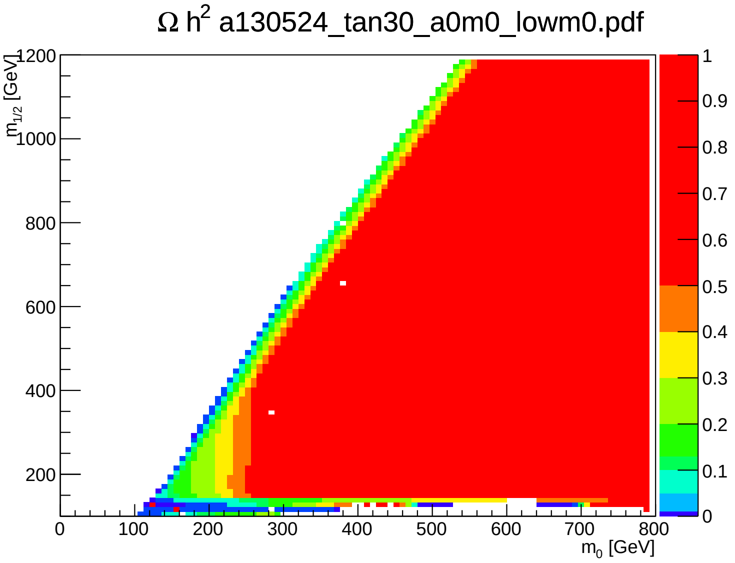

Figure 5.11: caption

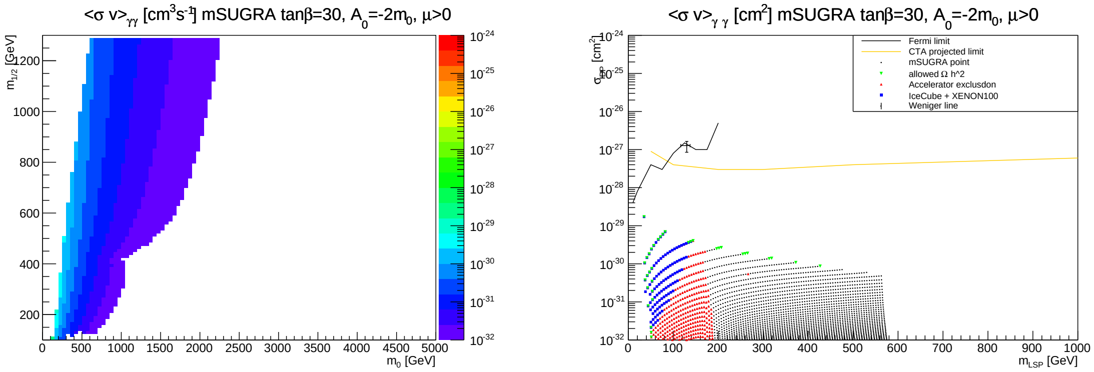

(a) $\langle \sigma v \rangle_{\gamma\gamma}$

(b) Fermi limit

Figure 5.12: The $\gamma\gamma$ coannihilation cross section computed by DarkSusy, with a comparison to the Fermi limit and a CTA projection.

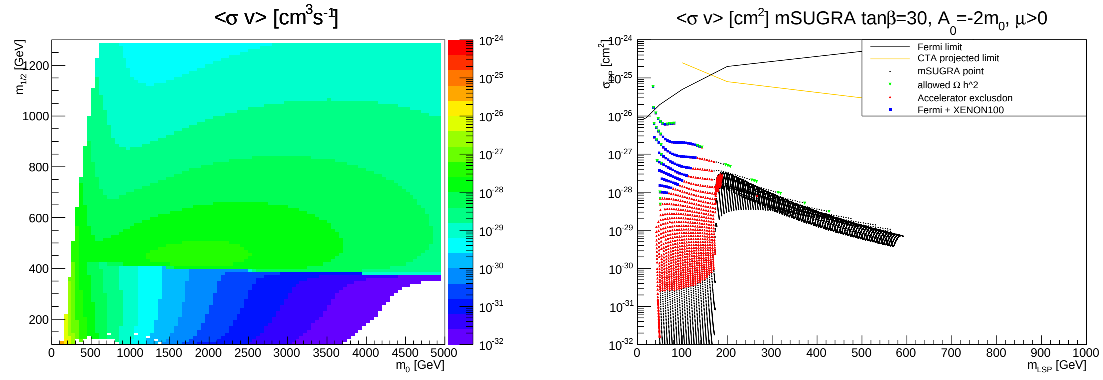

(a) $\langle \sigma v \rangle$ (b) Fermi limit

Figure 5.13: The total coannihilation cross section computed by DarkSusy 5.0.5, with a comparison to the Fermi limit and a CTA projection.

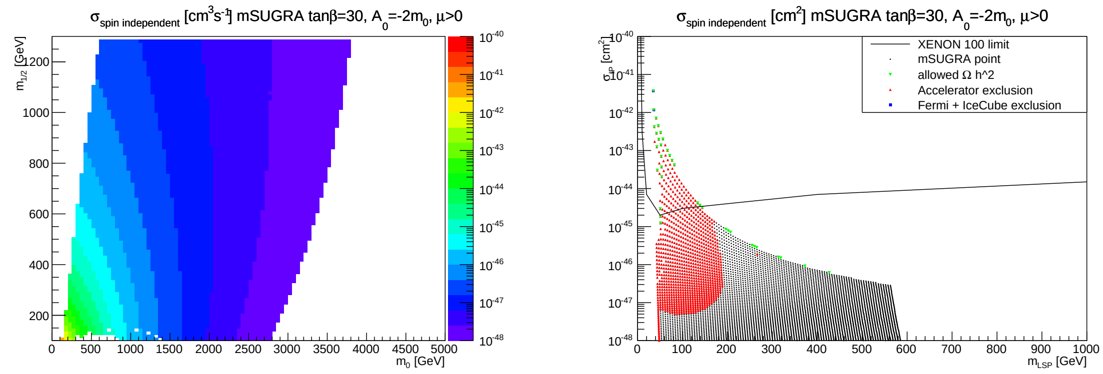

(a) $\sigma_{\text{independent}}$ (b) Xenon limit

Figure 5.14: The spin-independent neutralino-nucleon cross-section from DarkSusy 5.0.5, with a comparison to the XENON limit.

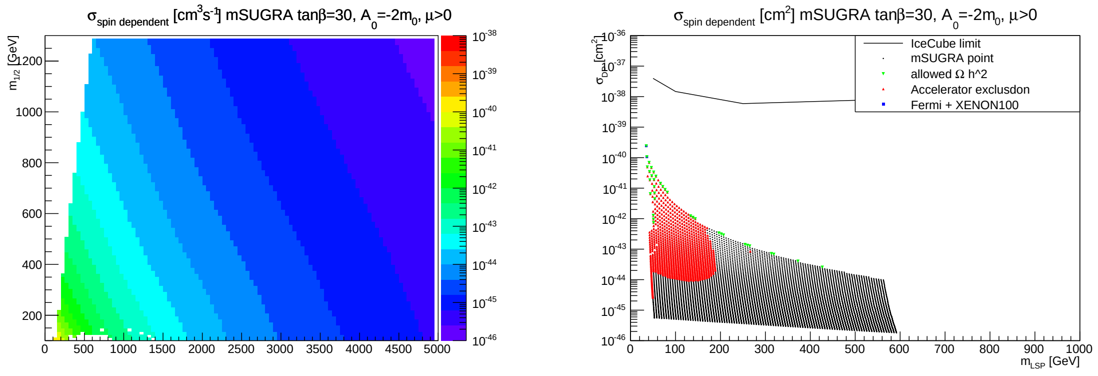

(a) $\sigma_{\text{dependent}}$

(b) IceCube limit

Figure 5.15: The spin-dependent neutralino-nucleon cross-section from DarkSusy 5.0.5, with a comparison to the IceCube limit.

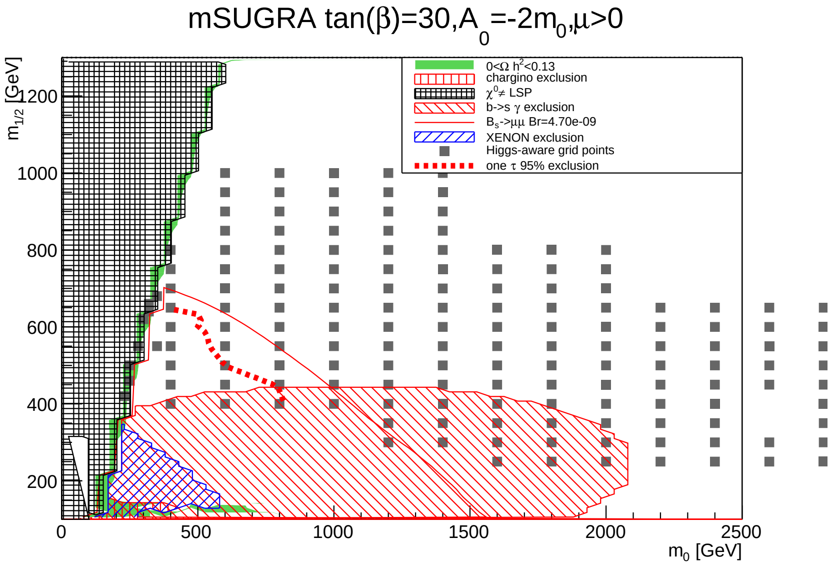

Figure 5.16: Exclusion contours, as well as a contour for the LHCB $B_s \rightarrow \mu^+/mu^-$. Points that are included in the ATLAS Higgs-aware grid are marked.

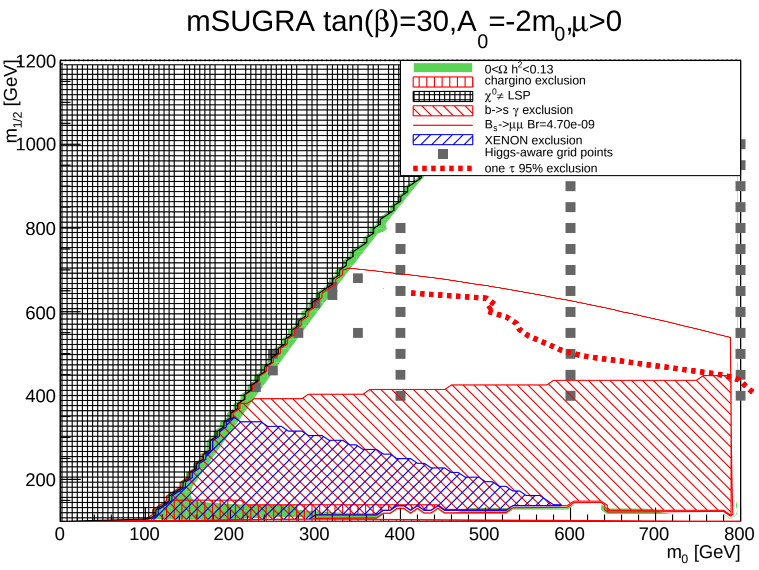

Figure 5.17: The same as Figure 5.16, but with a higher m_0 resolution.

5.3 Results from ALTAS search

5.3.1 Observed events

Three data events pass the analysis cuts. This may be compared with an expected number of $4.8 \pm 1.5 \pm 1.8$. No excess over the standard model is seen. Table 5.1 displays the cut-flow for data, background and some signal points.

After cut	Data $\sqrt{s} = 8$ TeV	All Std.Mod. backgrounds	GMSB $\Lambda = 60$, $\tan\beta = 30$	mSUGRA $m_0 = 400$, $m_{1/2} = 600$	mSUGRA $m_0 = 400$, $m_{1/2} = 650$
1 τ & no other lepton	14423	13460±529	22.4±0.9	45.7±1.6	21.9±0.7
$\Delta\Phi_{min} > 0.3$	13268	12646±482	18.1±0.8	38.2±1.5	17.5±0.6
met/meff> 0.3	8898	8279±313	7.4±0.5	20.5±1.0	10.4±0.5
$m_T > 140$GeV	401	460±130	4.7±0.4	13.1±0.9	6.51±0.37
$H_T > 800$GeV	3	4.8±1.5	1.9±0.3	11.0±0.8	5.62±0.34

Table 5.1: Cut-flow for background, data and some signal points. The expected numbers of events for all standard model backgrounds and for the example of one GMSB and two mSUGRA parameter space points correspond to an integrated luminosity of 20.7fb^{-1}.

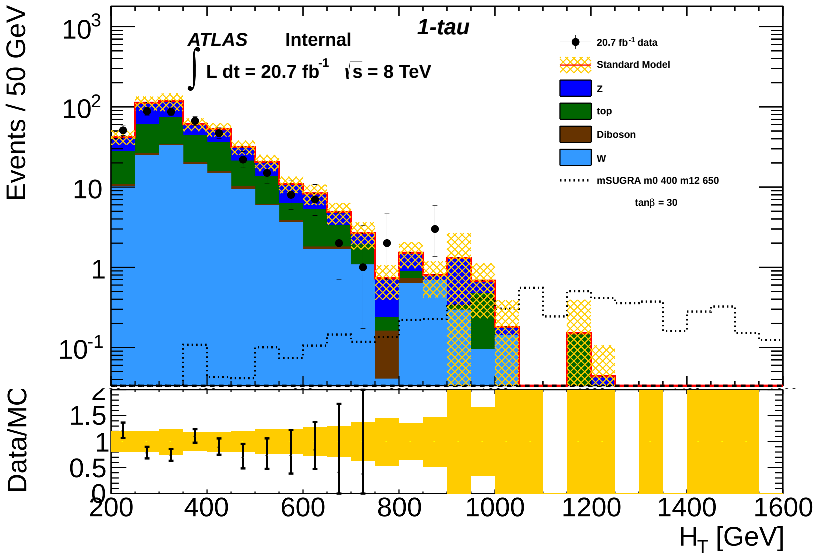

Figure 5.18: The unblinded H_T distribution. The three passed events, with $H_T = 850, 855, 881$ is easy to see as they have clustered in one bin.

5.3.2 Setting a limit

Given the estimates of the background and signal, as well as the uncertainties of both, the $1 - \tau$ analysis is able to set limits on what signal points have a low enough expectation value to be compatible with the data at 95% confidence level. The files from the signal analysis include each systematic uncertainty separately- so that if, for example, all signal and background contributions increase the same, the systematic background will not affect the exclusion contour. If that kind of systematic effect was just added in quadrature with all the others, the correlations between data sets, and possibly exclusion power would be lost.

The limit conforms well to the expected number of events seen in the analysis section. In response to the promise of excluding parts of the Higgs aware coannihilation region, it was decided to produce 9 extra points. These are the irregularly spaced markers in Figure 5.19. mSUGRA1taulimitorjan9points.pdf

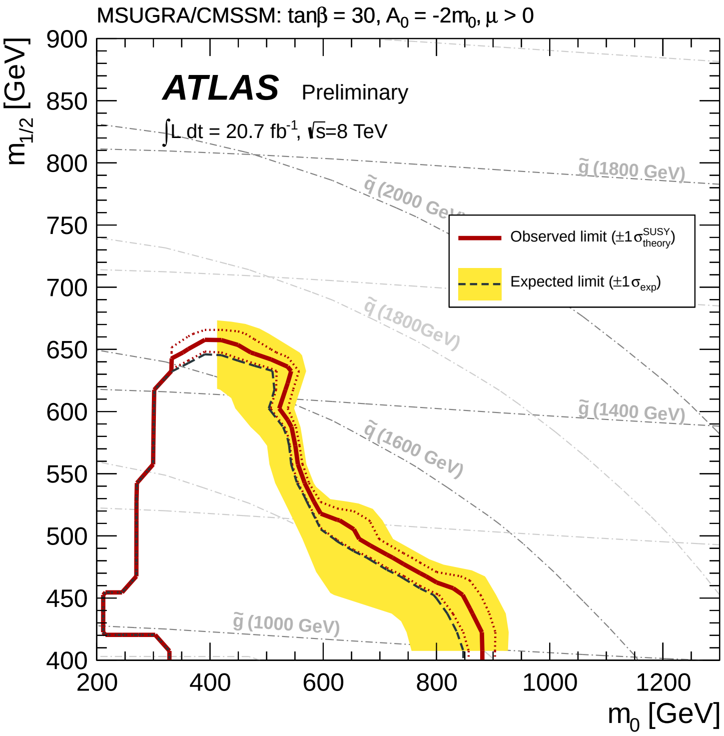

Figure 5.19: Exclusion contours from the one-tau analysis. The irregular spacing of the nine new points made plotting the uncertainties a challenge. Using the central value, however, and it is clear that the one-tau group has excluded parts of the coannihilation region. This also means that dark matter is excluded in the same region.

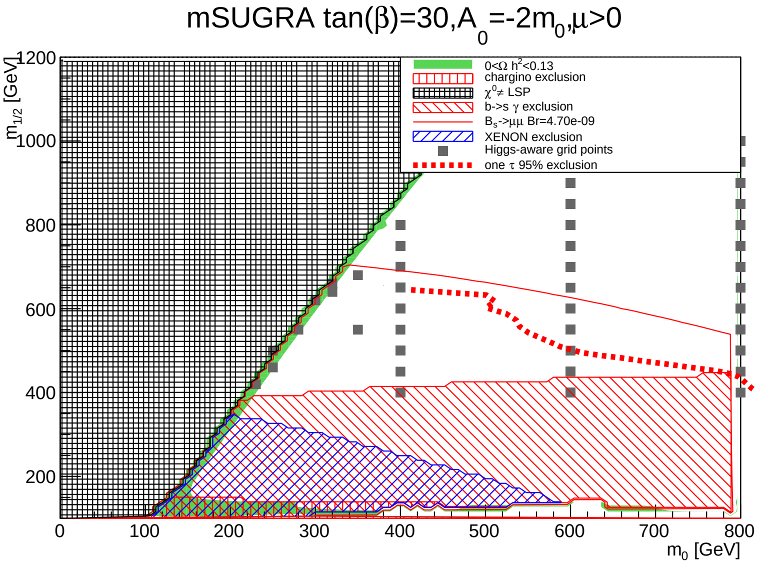

Figure 5.20: The nine new mSUGRApoints, close to and in the coannihilation region. The one tau exclusion curve is from *before* the nine new points is added as a dashed line. Figure 5.19 shows the entire exclusion plot

6

Conclusions

In this thesis, I have explored dark matter searches along three prongs.

First, I studied the Fermi-LAT exclusion limit in response to a dark matter coannihilation line. While the search did not utilize the powerful techniques of the original tentative discovery paper[70], a possible discovery of such magnitude warranted a thorough look at the method and data, especially when an investigation into the future exclusion power of CTA was being investigated.

The second was to compute variables of mSUGRAslices. The Higgs constraint is a strong one, but with the large parameter space of supersymmetry, there is always the option to extend the space and gain allowed quantities. The Non-Universal Higgs Mass scenario is essentially the mSUGRAwith a Higgs mass [22, p1428] as an input parameter. Together with other efforts [27], I have seen that some slices of mSUGRAhave yet to be excluded.

Third; I participated in an ATLAS search for supersymmetry. Included in the search was an mSUGRAgrid that was in much the same area of the parameter space as those slices that were considered in the previous part. In fact, when new points were added to the grid in response to the result, the analysis was able to impose limits in parts of the coannihilation region, which is also the most interesting area from the view of astrophysics.

This work follows a now long-established tradition of not finding supersymmetry. The parameter space of supersymmetry is vast, and with 124 parameters in play, it is hard to see that it could be ruled out in all versions. To search for supersymmetry, it becomes practical to either choose a simplified model, such as mSUGRA, or to focus on model-independent searches and measurements such as the Higgs mass.

That high energy physics has shaped the very largest and oldest structure of the universe is an awe-inspiring thought, and means that supersymmetry may be sought in the sky as well as at the LHC. Thus, the possible properties of dark matter in bulk may be measured or constrained; the relic density and the scattering and annihilation cross-sections.

During my work, the advantage of including such measurements in constraining supersymmetric models has become clear. Since they are simply one observable number given by the model, the process of computing their confidence limit for any sets of supersymmetric parameters is much more straightforward than computing a limit in supersymmetry. Searches for supersymmetry, and other models of physics beyond the standard model with large parameter spaces will benefit greatly if they let their choice of parameter points be guided by astrophysical observations.

The photon line in the Fermi Data, while tentative at the moment, would drastically influence physics. It would be the first evidence of physics beyond the standard model. It is also important to note that in the case of a discovery, both accelerators and astrophysical measurements will be needed to confirm the nature of dark matter.

As this thesis comes to an end, work is ongoing in the Efforts are underway to re-optimize the $1 - tau$ analysis with respect to the Higgs-aware signal grid. The Fermi collaboration, the Hess Cherenkov telescope, and the planned CTAwill all attempt to examine the reported gamma line.

Bibliography

[1] "Combined measurements of the mass and signal strength of the Higgs-like boson with the ATLAS detector using up to 25 fb^{-1} of proton-proton collision data". In: (2013).

[2] R Aaij et al. "First evidence for the decay Bs -> mu+ mu-". In: (2012). arXiv:`1211.2674 [Unknown]`.

[3] M.G. Aartsen et al. "Search for dark matter annihilations in the Sun with the 79-string IceCube detector". In: *Phys.Rev.Lett.* 110 (2013), p. 131302. DOI: `10.1103/PhysRevLett.110.131302`. arXiv:`1212.4097 [astro-ph.HE]`.

[4] M. Ackermann et al. "Constraints on the Galactic Halo Dark Matter from Fermi-LAT Diffuse Measurements". In: *Astrophys.J.* 761 (2012), p. 91. DOI: `10.1088/0004-637X/761/2/91`. arXiv:`1205.6474 [astro-ph.CO]`.

[5] M. Ackermann et al. "Fermi LAT Search for Dark Matter in Gamma-ray Lines and the Inclusive Photon Spectrum". In: *Phys.Rev.* D86 (2012), p. 022002. DOI: `10.1103/PhysRevD.86.022002`. arXiv:`1205.2739 [astro-ph.HE]`.

[6] M. Ackermann et al. "The Fermi Large Area Telescope On Orbit: Event Classification, Instrument Response Functions, and Calibration". In: *Astrophys.J.Suppl.* 203 (2012), p. 4. DOI: `10.1088/0067-0049/203/1/4`. arXiv:`1206.1896 [astro-ph.IM]`.

[7] P.A.R. Ade et al. "Planck 2013 results. XVI. Cosmological parameters". In: (2013). arXiv:`1303.5076 [astro-ph.CO]`.

[8] Andrea Albert. *Search for Gamma-ray Spectral Lines in the Milky Way Diffuse with the Fermi Large Area Telescope*. `fermi.gsfc.nasa.gov/science/mtgs/symposia/2012/program/.../AAlbert.pdf`. 2012.

[9] Donnino Anderhalden and Juerg Diemand. "Density Profiles of CDM Microhalos and their Implications for Annihilation Boost Factors". In: *JCAP* 1304 (2013), p. 009. DOI: `10.1088/1475-7516/2013/04/009`. arXiv:`1302.0003 [astro-ph.CO]`.

[10] I. Antcheva et al. "ROOT — A C++ framework for petabyte data storage, statistical analysis and visualization". In: *Computer Physics Communications* 182.6 (2011), pp. 1384 –1385. ISSN: 0010-4655. DOI: `10.1016/j.cpc.2011.02.008`. URL: `http://www.sciencedirect.com/science/article/pii/S0010465511000701`.

[11] ATLAS-SUSY-WG. *cross sections and their quoted references*. Tech. rep. Link: https://svnweb.cern.ch/trac Jan. 2013.

[12] W.B. Atwood et al. "The Large Area Telescope on the Fermi Gamma-ray Space Telescope Mission". In: *Astrophys.J.* 697 (2009), pp. 1071–1102. DOI: `10.1088/0004-637X/697/2/1071`. arXiv:`0902.1089 [astro-ph.IM]`.

[13] E. Barberio et al. "Averages of $b-$hadron properties at the end of 2006". In: (2007). arXiv:`0704.3575 [hep-ex]`.

[14] Vernon Barger, Wai-Yee Keung, and Gabe Shaughnessy. "Spin Dependence of Dark Matter Scattering". In: *Phys.Rev.* D78 (2008), p. 056007. DOI: `10.1103/PhysRevD.78.056007`. arXiv:`0806.1962 [hep-ph]`.

[15] Philip Bechtle et al. "HiggsBounds 2.0.0: Confronting Neutral and Charged Higgs Sector Predictions with Exclusion Bounds from LEP and the Tevatron". In: *Comput.Phys.Commun.* 182 (2011), pp. 2605–2631. DOI: `10.1016/j.cpc.2011.07.015`. arXiv:`1102.1898 [hep-ph]`.

[16] P Bechtle et al. *Search for Events with Large Missing Transverse Momentum, Jets, and Leptons (e/mu/tau) in 8 TeV Proton-Proton Collision Data with the ATLAS Detector*. Tech. rep. ATL-COM-PHYS-2012-1738. Geneva: CERN, Nov. 2012.

[17] Wim Beenakker et al. "Soft-gluon resummation for squark and gluino hadroproduction". In: *JHEP* 0912 (2009), p. 041. DOI: `10.1088/1126-6708/2009/12/041`. arXiv:`0909.4418 [hep-ph]`.

[18] W. Beenakker et al. "Squark and gluino hadroproduction". In: *Int.J.Mod.Phys.* A26 (2011), pp. 2637–2664. DOI: `10.1142/S0217751X11053560`. arXiv:`1105.1110 [hep-ph]`.

[19] W. Beenakker et al. “Squark and gluino production at hadron colliders”. In: *Nucl.Phys.* B492 (1997), pp. 51–103. DOI: `10.1016/S0550-3213(97)00084-9`. arXiv:`hep-ph/9610490 [hep-ph]`.

[20] K.G. Begeman, A.H. Broeils, and R.H. Sanders. “Extended rotation curves of spiral galaxies: Dark haloes and modified dynamics”. In: *Mon.Not.Roy.Astron.Soc.* 249 (1991), p. 523.

[21] Lars Bergstrom et al. “Investigating Gamma-Ray Lines from Dark Matter with Future Observatories”. In: *JCAP* 1211 (2012), p. 025. DOI: `10.1088/1475-7516/2012/11/025`. arXiv:`1207.6773 [hep-ph]`.

[22] J. Beringer et al. “Review of Particle Physics (RPP)”. In: *Phys.Rev.* D86 (2012), p. 010001. DOI: `10.1103/PhysRevD.86.010001`.

[23] Olga Bessidskaia. “Supersymmetric dark matter at the LHC and in non-collider experiments”. MA thesis. University of Stockholm, 2012.

[24] A. Bosma. “Dark matter in disc galaxies”. In: (1998). arXiv:`astro-ph/9812013 [astro-ph]`.

[25] Amos Breskin and Rüdinger Voss, eds. *The CERN Large Hadron Collider: Accelerator and Experiments*. Vol. 1. CERN, 2009.

[26] Trygve Buanes et al. “Sensitivity for observing dark matter through a gamma line emission from the galactic centre region with Cherenkov Telescope Array”. On behalf of the CTA collaboration, To be submitted.

[27] Thomas Burgess et al. “Finding viable Models in SUSY Parameter Spaces with Signal Specific Discovery Potential”. In: (2012). arXiv:`1210.7020 [hep-ph]`.

[28] Davide Cadamuro. “Cosmological limits on axions and axion-like particles”. In: (2012). arXiv:`1210.3196 [hep-ph]`.

[29] M. Chernyakova et al. “The high-energy, Arcminute-scale galactic center gamma-ray source”. In: *Astrophys.J.* 726 (2011), p. 60. DOI: `10.1088/0004-637X/726/2/60`. arXiv:`1009.2630 [astro-ph.HE]`.

[30] *Cicerone*. `http://fermi.gsfc.nasa.gov/ssc/data/analysis/documentation/Cicerone/Cicerone_Data/LAT_DP.html`. May 2013.

[31] Douglas Clowe et al. “A direct empirical proof of the existence of dark matter”. In: *Astrophys.J.* 648 (2006), pp. L109–L113. DOI: `10.1086/508162`. arXiv:`astro-ph/0608407 [astro-ph]`.

[32] Glen Cowan. *Expected discovery significance for counting experiment with background uncertainty*. `www.pp.rhul.ac.uk/~cowan/atlas/cowan_statforum_8may12.pdf`. 2012.

[33] G. Cowan et al. "Asymptotic Formulae for Likelihood-Based Tests of new Physics". In: *Eur. Phys. J.* C71 (2011), p. 1554. eprint: `arXiv:1007.1727`.

[34] *Data Policy Data Access Data Analysis + System Overview + Software Download + Documentation + Cicerone + Analysis Threads + User Contributions Caveats Newsletters FAQ LAT Data Selection Recommendatio*. `http://fermi.gsfc.nasa.gov/ssc/data/analysis/documentation/Cicerone/Cicerone_Data_Exploration/Data_preparation.html`. May 2013.

[35] G. Degrassi et al. "Towards high precision predictions for the MSSM Higgs sector". In: *Eur.Phys.J.* C28 (2003), pp. 133–143. DOI: `10.1140/epjc/s2003-01152-2`. arXiv:`hep-ph/0212020 [hep-ph]`.

[36] Abdelhak Djouadi. "The Anatomy of electro-weak symmetry breaking. II. The Higgs bosons in the minimal supersymmetric model". In: *Phys.Rept.* 459 (2008), pp. 1–241. DOI: `10.1016/j.physrep.2007.10.005`. arXiv:`hep-ph/0503173 [hep-ph]`.

[37] Abdelhak Djouadi, Manuel Drees, and Jean-Loic Kneur. "Neutralino dark matter in mSUGRA: Reopening the light Higgs pole window". In: *Phys.Lett.* B624 (2005), pp. 60–69. DOI: `10.1016/j.physletb.2005.08.010`. arXiv:`hep-ph/0504090 [hep-ph]`.

[38] Jaan Einasto. "Kinematics and dynamics of stellar systems". In: *Trudy Inst. Astrofiz. Alma-Ata* 51 (1965).

[39] M. Frank et al. "The Higgs Boson Masses and Mixings of the Complex MSSM in the Feynman-Diagrammatic Approach". In: *JHEP* 0702 (2007), p. 047. DOI: `10.1088/1126-6708/2007/02/047`. arXiv:`hep-ph/0611326 [hep-ph]`.

[40] Herbert Goldstein, Charles P. Poole Jr., and John L. Safko. *Classical Mechanics*. 3rd. Pearson Education International, 2002.

[41] P. Gondolo et al. "DarkSUSY: Computing supersymmetric dark matter properties numerically". In: *JCAP* 0407 (2004), p. 008. DOI: `10.1088/1475-7516/2004/07/008`. arXiv:`astro-ph/0406204 [astro-ph]`.

[42] P Gondolo et al. *DarkSUSY Manual and long description of routines*.

[43] K. M. Górski et al. "HEALPix: A Framework for High-Resolution Discretization and Fast Analysis of Data Distributed on the Sphere". In: *Astrophys.J.* 622 (Apr. 2005), pp. 759–771. DOI: `10.1086/427976`. eprint: `arXiv:astro-ph/0409513`.

[44] David J. Griffiths. *Introduction to Elementary Particles*. Wiley, 2008.

[45] S. Heinemeyer, W. Hollik, and G. Weiglein. "FeynHiggs: A Program for the calculation of the masses of the neutral CP even Higgs bosons in the MSSM". In: *Comput.Phys.Commun.* 124 (2000), pp. 76–89. DOI: `10.1016/S0010-4655(99)00364-1`. arXiv:`hep-ph/9812320 [hep-ph]`.

[46] S. Heinemeyer, W. Hollik, and G. Weiglein. "The Masses of the neutral CP - even Higgs bosons in the MSSM: Accurate analysis at the two loop level". In: *Eur.Phys.J.* C9 (1999), pp. 343–366. DOI: `10.1007/s100529900006`. arXiv:`hep-ph/9812472 [hep-ph]`.

[47] E. Hubble. "A Relation between Distance and Radial Velocity among Extra-Galactic Nebulae". In: *Proceedings of the National Academy of Science* 15 (Mar. 1929), pp. 168–173. DOI: `10.1073/pnas.15.3.168`.

[48] F. James. *MINUIT*. CERN Program Library Long Writeup D506, 1994.

[49] Michael Kramer et al. "Supersymmetry production cross sections in pp collisions at $\sqrt{s} = 7$ TeV". In: (2012). arXiv:`1206.2892 [hep-ph]`.

[50] A. Kulesza and L. Motyka. "Soft gluon resummation for the production of gluino-gluino and squark-antisquark pairs at the LHC". In: *Phys.Rev.* D80 (2009), p. 095004. DOI: `10.1103/PhysRevD.80.095004`. arXiv:`0905.4749 [hep-ph]`.

[51] A. Kulesza and L. Motyka. "Threshold resummation for squark-antisquark and gluino-pair production at the LHC". In: *Phys.Rev.Lett.* 102 (2009), p. 111802. DOI: `10.1103/PhysRevLett.102.111802`. arXiv:`0807.2405 [hep-ph]`.

[52] LEPSUSYWG, ALEPH, DELPHI, L3 and OPAL experiments. *note LEPSUSY/02-04.1*. `http://lepsusy.web.cern.ch/lepsusy/Welcome.html`.

[53] LEPSUSYWG, ALEPH, DELPHI, L3 and OPAL experiments. *note LEPSUSY/04-01.1*. `http://lepsusy.web.cern.ch/lepsusy/Welcome.html`.

[54] *LuminosityPublicResults*. `https://twiki.cern.ch/twiki/bin/view/AtlasPublic/LuminosityPublicResults#2012_pp_Collisions`. May 2013.

[55] Franz Mandl and Graham Shaw. *Quantum Field Theory*. 2nd ed. Wiley, 2010.

[56] Stephen Martin, Tapas Sarangi, and Xavier Portell. *Considering Scenarios with Higgs Constraints*. `https://indico.cern.ch/getFile.py/access?contribId=14&sessionId=1&resId=0&materialId=slides&confId=188153`.

[57] M. Misiak et al. "Estimate of B(anti-B —>; X(s) gamma) at O(alpha(s)**2)". In: *Phys.Rev.Lett.* 98 (2007), p. 022002. DOI: `10.1103/PhysRevLett.98.022002`. arXiv:`hep-ph/0609232 [hep-ph]`.

[58] A.A. Moiseev et al. "The anti-coincidence detector for the {GLAST} large area telescope". In: *Astroparticle Physics* 27.5 (2007), pp. 339 –358. ISSN: 0927-6505. DOI: `10.1016/j.astropartphys.2006.12.003`. URL: `http://www.sciencedirect.com/science/article/pii/S0927650506001885`.

[59] Jan Myrheim. *Classical Theory of Fields*. Compendium for the course Gravitation and Cosmology at NTNU. 2011.

[60] K. Nakamura et al. *Particle Physics Booklet*. IOP Publishing, 2010.

[61] Julio F. Navarro et al. "The Diversity and Similarity of Cold Dark Matter Halos". In: (2008). arXiv:`0810.1522 [astro-ph]`.

[62] *Observation of an Excess of Events in the Search for the Standard Model Higgs boson with the ATLAS detector at the LHC*. Tech. rep. ATLAS-CONF-2012-093. Geneva: CERN, July 2012.

[63] Frank E. Paige et al. ISAJET *7.83 A Monte Carlo Event Generator for pp, $\bar{p}p$ and e^+e^- Reactions*.

[64] D. H. Perkins. *Particle Astrophysics*. Oxford University Press, 2009.

[65] *PileupReweighting*. `https://twiki.cern.ch/twiki/bin/viewauth/AtlasProtected/PileupReweighting`. May 2013.

[66] Stefano Profumo. "The Quest for Supersymmetry: Early LHC Results versus Direct and Indirect Neutralino Dark Matter Searches". In: *Phys.Rev.* D84 (2011), p. 015008. DOI: `10.1103/PhysRevD.84.015008`. arXiv:`1105.5162 [hep-ph]`.

[67] *SUSYSignalUncertainties*. `"https://twiki.cern.ch/twiki/bin/viewauth/AtlasProtected/SUSYSignalUncertainties#Details_on_the_Calculation_of_cr"`. May 2013.

[68] Gilles Vertongen and Christoph Weniger. "Hunting Dark Matter Gamma-Ray Lines with the Fermi LAT". In: *JCAP* 1105 (2011), p. 027. DOI: `10.1088/1475-7516/2011/05/027`. arXiv:`1101.2610 [hep-ph]`.

[69] A. W. van der Waart. *Asymptotic Statistics*. Cambridge Series in Statistical and Probabilistic Mathematics. Cambridge University Press, 1998.

[70] Christoph Weniger. "A Tentative Gamma-Ray Line from Dark Matter Annihilation at the Fermi Large Area Telescope". In: *JCAP* 1208 (2012), p. 007. DOI: `10.1088/1475-7516/2012/08/007`. arXiv:`1204.2797 [hep-ph]`.

[71] B. M. H. R. Wevers, P. C. van der Kruit, and R. J. Allen. "The Palomar-Westerbork survey of northern spiral galaxies". In: *Astronomy and Astrophysics Supplement Series* 66.4 (Dec. 1986), pp. 505–513.

[72] L. Wyrzykowski et al. "The OGLE View of Microlensing towards the Magellanic Clouds. IV. OGLE-III SMC Data and Final Conclusions on MACHOs". In: (2011). arXiv:`1106.2925 [astro-ph.GA]`.

[73] F. Zwicky. "Die Rotverschiebung von extragalaktischen Nebeln". In: *Helvetica Physica Acta* 6 (1933), pp. 110–127.

Appendix A

Computer Programs

A.1 Software Acknowledgments

During my work, I have used many computer programs and packages. Much of the work I have done would be slower or even impossible to accomplish in time if these tools were not provided freely to the scientific community.

- Fermi Science Tools
- Python
- C++
- Root
- Minuit

- Fortran
- Healpix
- Healpy
- numpy
- LaTeX
- pyfits

The LaTeXtemplate used for the thesis was made by Alexander Skjæveland Larsen `https://github.com/ogrim/uib-latex`

Appendix B

ATLASsupporting material

B.1 Signal Samples

Sample ID	m_0	$m_{1/2}$	σ_{total} [pb]	Sample ID	m_0	$m_{1/2}$	σ [pb]
166732	400	400	0.363	166769	1000	600	0.00693
166733	400	450	0.173	166770	1000	650	0.00373
166734	400	500	0.0843	166771	1000	700	0.00198
166735	400	550	0.0424	166772	1000	750	0.00108
166736	400	600	0.0217	166773	1000	800	0.000594
166737	400	650	0.0111	166774	1000	850	0.000327
166738	400	700	0.00595	166775	1000	900	0.000180
166739	400	750	0.00310	166776	1000	950	9.99e-05
166740	400	800	0.00169	166803	1000	1000	5.56e-05
166741	600	400	0.244	166948	1200	300	0.657
166742	600	450	0.1179	166938	1200	350	0.243
166743	600	500	0.0580	166777	1200	400	0.0989
166744	600	550	0.0296	166778	1200	450	0.0437
166745	600	600	0.0153	166779	1200	500	0.0205
166746	600	650	0.00801	166780	1200	550	0.0101
166747	600	700	0.00429	166781	1200	600	0.00511
166748	600	750	0.00233	166782	1200	650	0.00267
166749	600	800	0.00126	166783	1200	700	0.00142
166750	600	850	0.000654	166784	1200	750	0.000766
166751	600	900	0.000371	166785	1200	800	0.000418
166752	600	950	0.000200	166786	1200	850	0.000230
166801	600	1000	0.000110	166787	1200	900	0.000128
166753	800	400	0.167	166788	1200	950	7.08e-05
166754	800	450	0.0787	166804	1200	1000	3.97e-05
166755	800	500	0.0388	166949	1400	300	0.525
166756	800	550	0.0198	166950	1400	350	0.201
166757	800	600	0.0103	166789	1400	400	0.0832
166758	800	650	0.00549	166790	1400	450	0.0366
166759	800	700	0.00295	166791	1400	500	0.0169
166760	800	750	0.00160	166792	1400	550	0.00818
166761	800	800	0.000872	166793	1400	600	0.00408
166762	800	850	0.000477	166794	1400	650	0.00209
166763	800	900	0.000247	166795	1400	700	0.00110
166764	800	950	0.000144	166796	1400	750	0.000587
166802	800	1000	7.96e-05	166797	1400	800	0.000319
166765	1000	400	0.123	166798	1400	850	0.000175
166766	1000	450	0.0561	166799	1400	900	9.65e-05
166767	1000	500	0.0270	166800	1400	950	5.38e-05
166768	1000	550	0.0134	166805	1400	1000	3.03e-05

Table B.1: List of MC samples for the SUSY signal in the mSUGRA Higgs boson-aware grid. Masses are quoted in GeV. Another 105 samples with $m_0 > 2000$ GeV have been generated, but they are far away from the region where the $\tilde{\tau}$is the NLSP.

Sample ID	m_0	$m_{1/2}$	σ [pb]
166951	280	550	0.051
166952	300	620	0.019
166953	320	640	0.014
166954	320	660	0.011
166955	350	550	0.047
166956	350	680	0.0083
166957	230	420	0.36
166958	250	460	0.19
166959	250	500	0.11

Table B.2: List of nine additional MC samples close to the coannihilation region for the SUSY signal in the mSUGRA Higgs boson-aware grid. Masses are quoted in GeV.